# ASACUSA STATUS REPORT

## ASACUSA progress during 2010
## and plans for 2011

## ASACUSA collaboration

D. Barna[1,6], M. Charlton[2], M. Corradini[3], A. Dax[1], Y. Enomoto[5],
S. Federmann[8], S. Friedreich[8], R.S. Hayano[1], H. Higaki[5], M. Hori[1,11], D. Horváth[6],
C.A. Hunniford[9], B. Juhász[8], Y. Kanai[5], C. Kim[4], H. Knudsen[7], H-P. Kristiansen[7],
T. Kobayashi[1], N. Kuroda[4], M. Leali[3], E. Lodi-Rizzini[3], M. Lund[7], V. Mascagna[3], O. Massiczek[8],
Y. Matsuda[4], R.W. McCullough[9], K. Michishio[5], S.P. Møller[7], T. Pask[8], W. Pirkl[1],
A. Sótér[11], K. Todoroki[1], K. Tőkési[10], H.D. Thomsen[7], H.A. Torii[4], U. Uggerhøj[7], L. Venturelli[3],
E. Widmann[8], Y. Yamazaki[5], P. Zalán[6], J. Zmeskal[8], N. Zurlo[3]

1. The University of Tokyo (JP), 2. University of Swansea (GB), 3. Università di Brescia and INFN (IT),
4. The University of Tokyo, Komaba (JP), 5. RIKEN (JP), 6. KFKI (HU), 7. University of Aarhus (DK),
8. Stefan Meyer Institute (AT), 9. The Queen's University of Belfast (UK),
10. ATOMKI (HU), 11 Max-Planck-Institut für Quantenoptik (DE)

# Executive Summary

**H̄ atom formation in the cusp trap**

1. By mixing some $3 \times 10^5$ antiprotons with $3 - 5 \times 10^6$ positrons in the "cusp" trap, we observed about 70 H̄ atoms per mixing, in high Rydberg states of $n \sim 45 - 50$ (published in PRL [1]). This would correspond to about $7 \times 10^3$ H̄ per mixing assuming an isotropic angular distribution (i.e., $\bar{p} \to \bar{H}$ conversion efficiency of $\sim 2\%$).

2. In 2011, we will first use the same setup as in 2010, and attempt to extract H̄ atoms, and to optimize the extracted H̄ yield.

3. We will then install a microwave cavity and a sextupole magnet downstream of the cusp trap, and start the microwave spectroscopy of the ground state hyperfine transitions of H̄ atoms.

**First laser-spectroscopy of ultra-cold antiprotonic helium atoms**

4. We succeeded to cool $\bar{p}\text{He}^+$ atoms to temperature $T \sim 1.5$ K by employing the technique of gas buffer cooling in dilute helium gas, and improved the theory-experiment agreement in the single-photon laser transition frequencies from $1 - 3$ parts in $10^8$ to $5 - 6$ parts in $10^9$ for seven transitions in the $\bar{p}^4\text{He}$ and $\bar{p}^3\text{He}$ atoms.

5. In 2011, we will extend the measurements to all other accessible transitions in $^3\text{He}$ and in $^4\text{He}$ ($12 - 14$ transitions in total including the ones we measured in 2010). When completed, the precision of the $m_{\bar{p}}$-to-$m_e$ ratio will improve by a factor $\sim 4$ over the previous (2006) value.

**Antiprotonic helium-3 microwave spectroscopy**

6. The antiprotonic helium-3 hyperfine splitting was observed for the first time. This is for two of the four microwave transitions of the $(n, l) = (36, 34)$ state of $\bar{p}^3\text{He}$ at 11 GHz. The measured transition frequencies are $11.12559 \pm 0.00014$ GHz and $11.15839 \pm 0.00018$ GHz, agreeing with theory within less than 1 MHz.

7. In 2011, we plan to gain statistics for the two 11 GHz transitions, in order to further test the 3-body QED theories. We will also measure the other two transitions at 16 GHz for the first time, by changing the target/cavity assembly.

**Atomic and nuclear collision experiments**

8. We completed the measurement of the cross section for single, non-dissociative ionization of molecular hydrogen for antiproton impact in the energy range $2 - 11$ keV (published in PRL [20]). The molecular cross section is proportional to the projectile velocity, and is unexpectedly small; temporary formation of a $H^-$-like system is considered to be the reason for this unexpected behaviour. In the future, we plan to measure differential cross sections using a "reaction microscope".

9. Antiproton annihilation cross section was measured for the first time at 100 keV in carbon. In 2011, we extend the measurements to heavier targets (Ni, Sn, Pt) with an improved setup, so as to study the $A$ dependence.

# ASACUSA Beam usage plan for 2011

| | |
|---|---|
| "CUSP" trap - antihydrogen beam extraction | 10 weeks |
| Antiprotonic helium laser spectroscopy | 7 weeks |
| Antiprotonic helium-3 microwave resonance | 7 weeks |
| Antiproton-nucleus annihilation cross section at 100 keV | 2 weeks |
| Total = 28 weeks - AD4 - AEGIS $\sim$ 26 weeks | |

# Contents

# 1 Achievement of the cusp trap experiment

We succeeded in synthesizing $\bar{\text{H}}$ atoms in the cusp trap with a configuration shown in fig. 1, where $\bar{p}$ as well as $e^+$ were both injected from upstream (top right) of the cusp trap [1]. By this way, we can extracted an $\bar{\text{H}}$ beam downstream of the cusp trap, which can be monitored by an $\bar{\text{H}}$ detector, the important step to the microwave spectroscopy to be pursued in 2011 and beyond.

To improve the basic performance of the cusp trap, we added two more non-evaporable getter (NEG) pumps, and thermal contacts of multiple ring electrodes (MRE) and radiation shields were modified to keep the cusp trap region at lower temperature. These treatments are particularly effective to reduce the partial pressure of $H_2$ residual gas. Now, a typical life time of $\bar{p}$s in the cusp trap were 7000 s or longer, which is compared with $\sim$ 500 s last year.
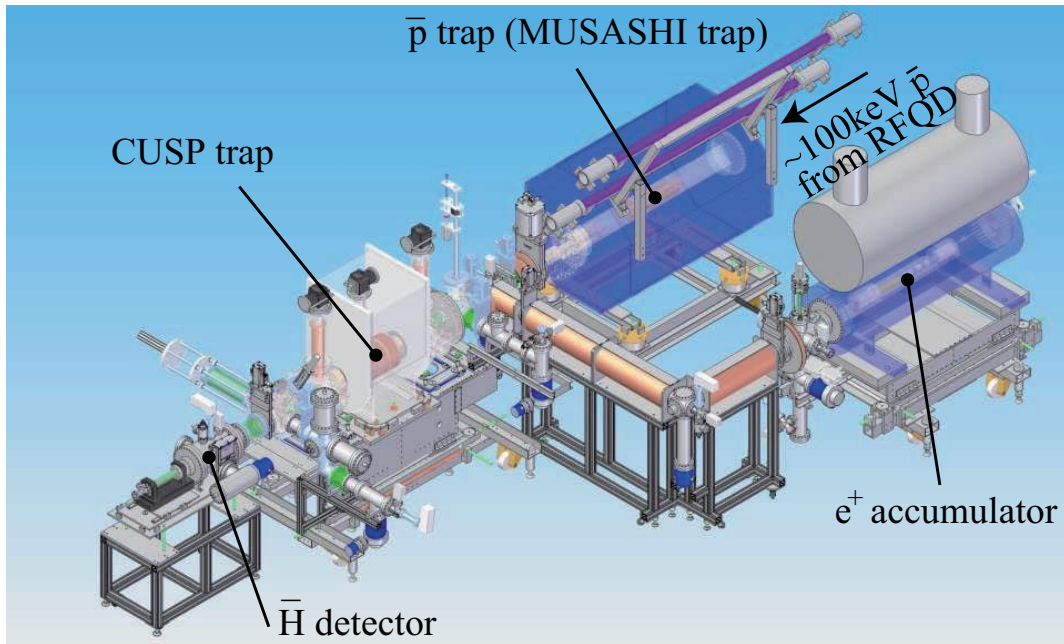


**Figure 1:** *Layout of MUSASHI trap, Positron accumulator, cusp trap and $\bar{\text{H}}$ detector.*

## 1.1 AD condition and MUSASHI $\bar{p}$ trap

At the beginning of the AD run in May 2010, $\bar{p}$ beams were stable and strong, we succeeded to capture $1.5 \times 10^6$ $\bar{p}$s per one AD shot, which is one of the best records. Actually, more than $10^7$ $\bar{p}$s were accumulated just by stacking seven AD shots. Unfortunately, the AD condition got less favorable with respect to the beam intensity, the emittance, and the bunch length in the rest of the beamtime. The number of $\bar{p}$s captured per one AD shot was quite limited like $7$–$8 \times 10^5$ $\bar{p}$s. In 2010, MUSASHI [2] provided 150 eV 2 $\mu$s pulsed beam $\bar{p}$s to the cusp trap, and 20–30 s DC-like beam at 250 eV for the AIA experiment.

## 1.2 Positron Accumulator

Low energy positrons for the production of anti-hydrogen atoms in the cusp trap are prepared in following three steps (see also fig. 1).

1) Accumulate low energy positrons in the e$^+$ accumulator.

2) Transfer the accumulated positrons to the cusp trap as a pulse via a positron beamline.

3) Make multiple stacking into the cusp trap and control the density of a positron plasma for the efficient production of anti-hydrogen atoms.

### 1.2.1  e$^+$ Accumulator

The structure of the e$^+$ accumulator is basically the same as the last year. Fast positrons from a 27-mCi $^{22}$Na radioactive source housed in a radiation shield made of W alloy were epi-thermalized with a pair of polycrystalline W moderators on both sides of the positron MRE, degraded by a N$_2$ gas-buffer cell, and finally accumulated in the positron MRE. It is noted that all the components described above are in a superconducting solenoid operated at 2.5T. Such an all-in-one system in the strong magnetic field has several advantages such as a stable trapping by suppressing diffusion and a rapid cooling of positrons by synchrotron radiation ($\propto 1/B^2$, where $B$ is the magnetic field) in the strong magnetic field. A half of positrons emitted from the source are automatically guided to the main trapping region following the magnetic field lines. Further, as positrons are extracted from the strong magnetic field region of the e$^+$ accumulator, the transport efficiency to the cusp trap can be very high without suffering reflection by the magnetic mirror effect.

Positrons are accumulated in a pseudo-harmonic potential near the exit of the positron MRE, where positrons have a lifetime of about 100 s [3]. By optimizing parameters (such as trapping potential, buffer gas pressure, moderator treatments, axial alignment of the MRT with respect to the magnetic field, etc.), about 10$^6$ positrons were accumulated in 100 s. Typically, $2\times10^5$ positrons were accumulated every 30 s. During the beam time, the e$^+$-accumulator was operated every 50 s to maximize the number of positrons in the cusp trap per unit time.

### 1.2.2  Positron transfer

In order to inject positrons in the cusp trap from the upstream side, a new beam line was designed by calculating their trajectories with CST Studio (CST Computer Simulation Technology AG). Since the energy of the positrons is typically less than 200 eV and there is a weak magnetic field leaking from other two superconducting magnets, a magnetic field is expected to be more efficient than electrostatic transport. Figure 2 (a) is a top view of the whole setup with trajectories of 100 eV positrons extracted from the e$^+$ accumulator. Assuming that the perpendicular energy of positrons are less than 1 eV, 49 positrons are set at a 6 mm × 6 mm square on the axis of symmetry and ejected with pitch angles less than 0.6 degree. As is seen, positrons are successfully transferred. Figure 2 (b) is a photo of the transport line during installation. A movable beam monitor, a combination of an MCP, and a phosphor screen were installed in front of the cusp trap, so that the positron beam profile can be monitored. The monitor is also rotatable and it can be used to observe the profile and the charge of positrons extracted from the cusp trap. It was found that the optimum condition of the transport parameters was fairly well predicted by those calculations. The optimized transport efficiency was about 50 to 60 %. Beam profiles observed with the monitor revealed that the positron beam was scraped at two 90 degree corners, which indicated that the radius of the positron cloud in the e$^+$-accumulator was larger than 4.5 mm.

### 1.2.3  Positron manipulation in the cusp trap

As mentioned above, a pulsed positron beam is injected into the cusp trap through the new transport line and typically $\sim 1\times10^5$ positrons are captured in a harmonic (accumulation) potential formed in the cusp trap. Since the confinement time of positrons in the cusp trap is longer than 4000 s, multi-injection of positron
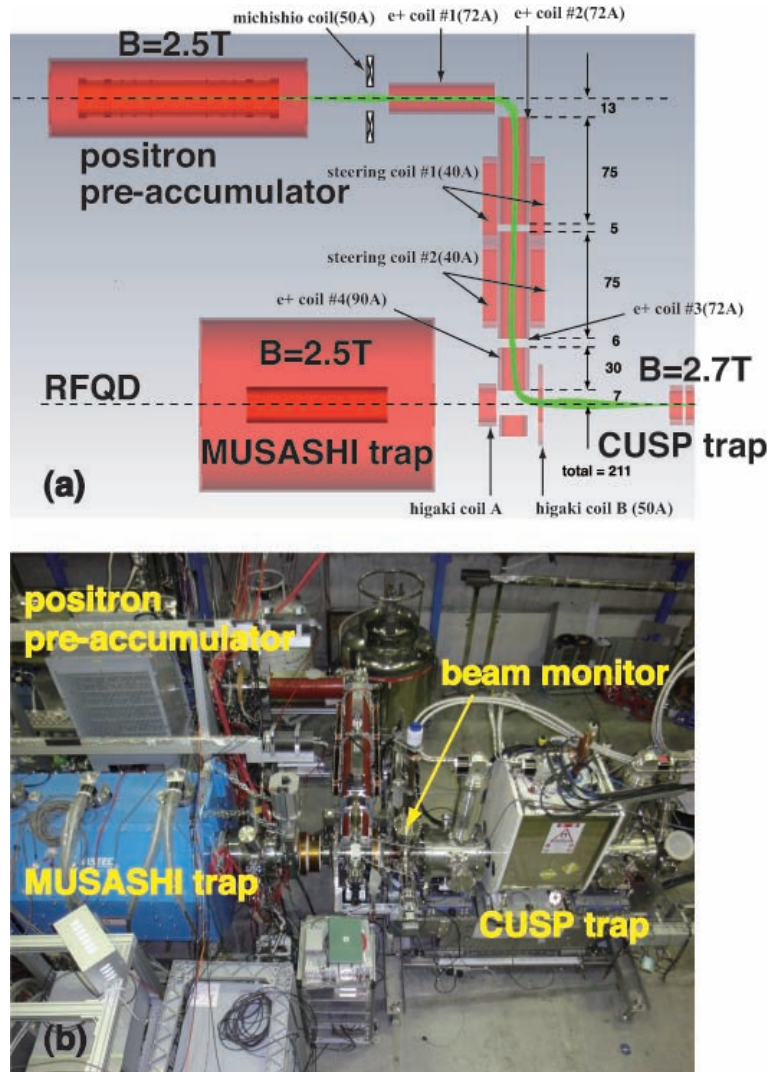
**Figure 2:** *(a) Trajectories of 100 eV positrons extracted from the positron source. (b) Positron transfer line during installation. A movable beam monitor is equipped in front of the cusp trap.*

pulses from the e$^+$-accumulator was performed to increase the number of positrons. Further, if the number of positrons becomes large and they behave as a plasma, rotating electric field can be applied to obtain the higher density [4].

Figure 3 (a) shows the number of positrons extracted from the cusp trap as a function of the stacking number of positrons. The number of positrons are measured by extracting them to the beam monitor at the upstream of the cusp trap. It is seen that the positron number increased almost linearly up to 60 stackings when the rotating electric field was applied during the stacking. On the other hand, when no rotation was applied, the number leveled off, i.e., the number of positrons stored in the cusp MRE increased linearly with the number of stackings, but the radial distribution expanded considerably and the number of positrons arriving the monitor increased weakly. The maximum number of positrons in the cusp trap was $6 \times 10^6$.

Figures 4 (a) and (b) show examples of the positron profiles without and with the rotating field, respectively. When no rotating electric field was applied, the image spread over an active area of the MCP, which is $\phi \sim 40$ mm. On the other hand, when the rotating electric field was applied, the positron cloud was sharply compressed as is seen in fig.4(b). The estimated diameter was $\phi \sim 6$ mm at the position of the beam monitor,
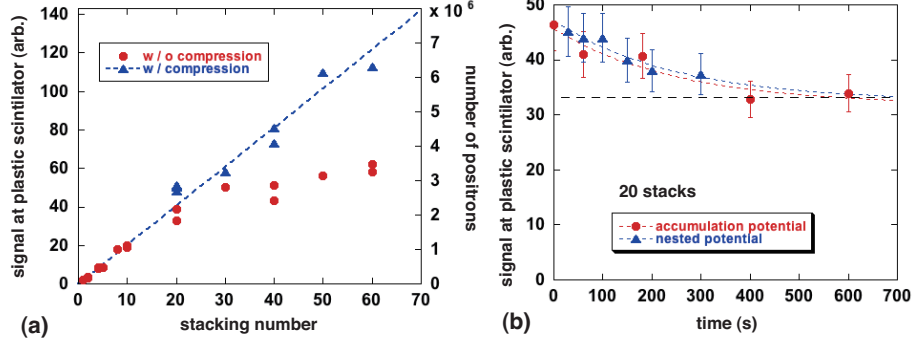
3

**Figure 3:** *(a) The number of positrons extracted from the cusp trap as a function of stacking number with (blue solid triangles) and without (red solid circles) radial compression. (b) The number of positrons as a function of time after the radial compression for a harmonic potential (red solid circles) and a nested trap potential (blue solid triangles).*
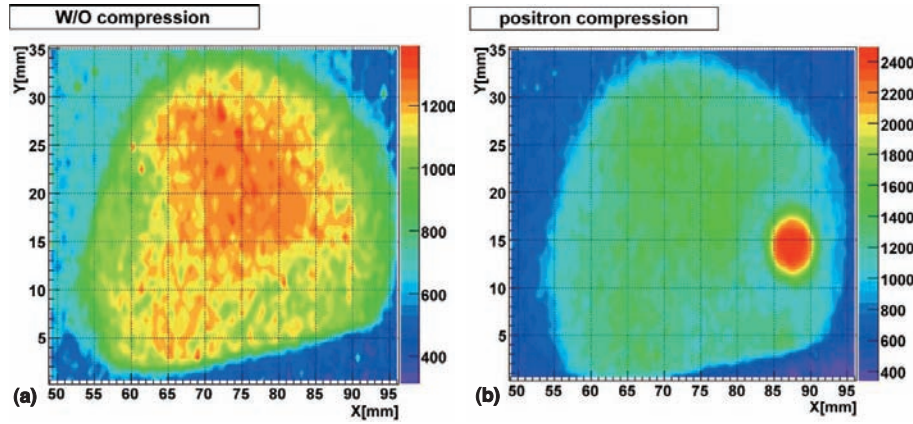


**Figure 4:** *Phosphor screen images of positrons extracted from the cusp trap (a) without radial compression and (b) with radial compression.*

which corresponded to the plasma diameter of about 1mm in the cusp trap and the density amounted to the order of $10^7$ cm$^{-3}$. Figure 3 (b) shows the number of positrons reached the beam monitor as a function of time after the compression, which revealed that the positron cloud expanded with a time constant of ∼250 s irrespective of the trapping potential (either harmonic or nested). It is also noted that the positron cloud can be repeatedly compressed by applying the rotating field even when the cloud expanded once.

In summary, a positron cloud composed of $6 \times 10^6$ positrons at maximum with the density close to $10^8$ cm$^{-3}$ was prepared in the cusp trap with the use of rotating electric field.

## 1.3 H̄ atom formation in the cusp trap

Figures 5 (a) and (b) show a cross-sectional view of the cusp trap including the H̄ detector superimposed magnetic field lines and a nested potential well configuration, respectively. As is seen, the nested trap was prepared at the upstream spindle region of the cusp magnetic field injecting $\bar{p}$ and $e^+$ from upstream. The number of $e^+$ stackings were typically 40–60 when H̄ synthesis was tried, which typically corresponded to 3–5 × 10$^6$$e^+$s. We applied the rotating field to maintain the radius of $e^+$ cloud small [5], which helped to realize longer lifetime and higher density (as high as ∼ $10^8$/cm$^3$) in the cusp trap. Then we prepared a nested potential configuration for syntheses of H̄ atoms [6] [7] [8] as shown in f ig. 5 (b) where the beam of $3 \times 10^5$$\bar{p}$s at the energy of 150 eV from MUSASHI trap were injected and mixed with the preloaded
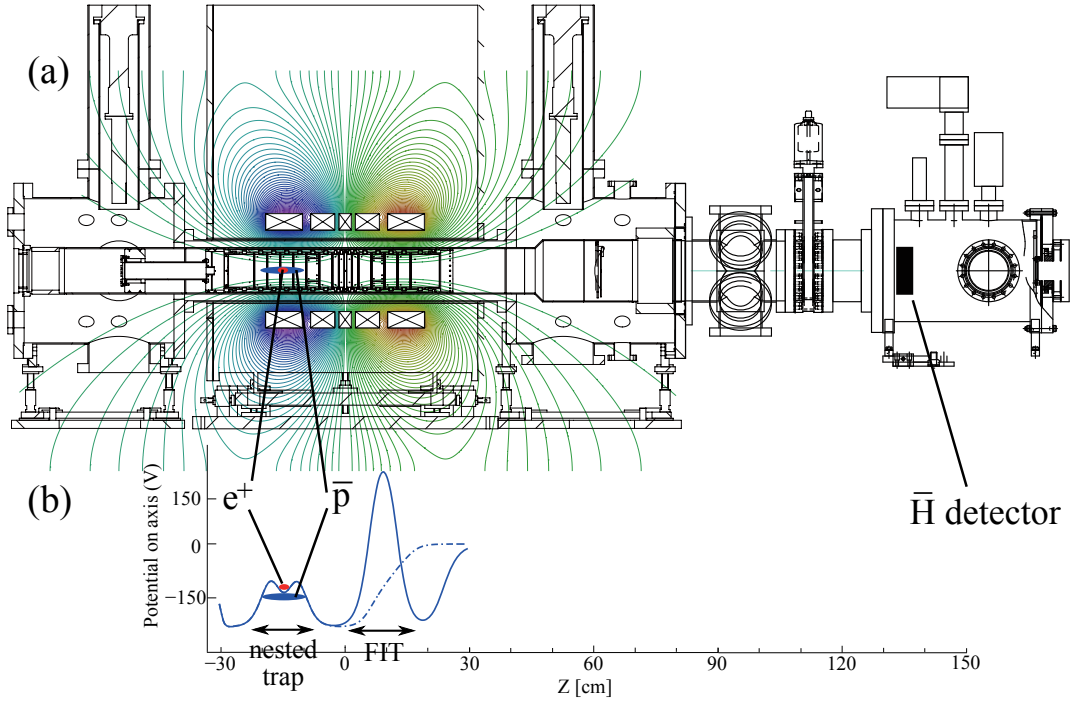
4

**Figure 5:** *(a) Schematic cross sectional view of cusp trap with H̄ detector. (b) A nested potential configuration along the axis is also shown.*
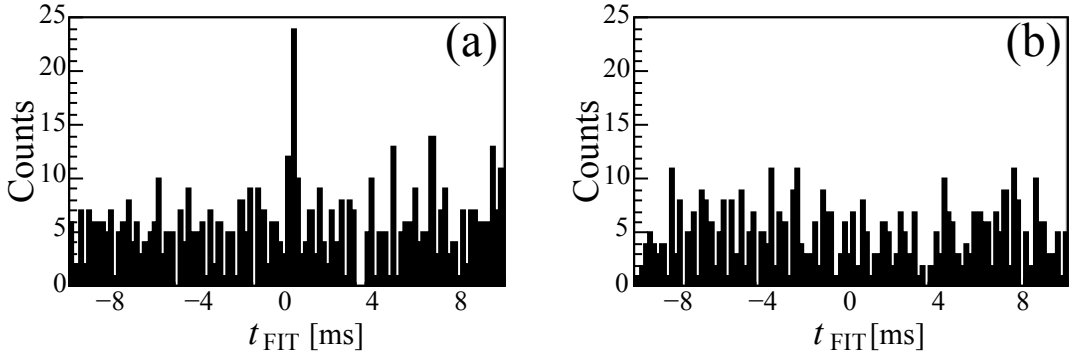


**Figure 6:** *The time spectra obtained by summing the spectra around the timing of the first ten FIT openings (a) with and (b) without $e^+$.*

$e^+$s. The $e^+$s were heated by injected $\bar{p}$s, then cooled via cyclotron (synchrotron) radiation, and eventually captured by $\bar{p}$s to form H̄ atoms. Although $\bar{p}$s in the nested well had no chance to move beyond the potential barrier, H̄ atoms which are neutral moved freely and a part of them reached the field-ionization trap (FIT). The H̄ atoms in high Rydberg states were field ionized and their $\bar{p}$s were accumulated in the FIT [7].

Figure 6 shows counts from the 3D track detector during the mixture of $\bar{p}$ (a) with and (b) without $e^+$. It is seen that a sharp peak with a fraction of ms in width appeared at the timing when the FIT was opened ($t_{\mathrm{FIT}} = 0$) only if $e^+$s were in the nested trap. The background was primarily due to cosmic rays and annihilation of trapped $\bar{p}$s with the residual gas. We also attempted to suppress $\bar{p}$ annihilation by heating up $e^+$ plasma with a RF field [9], then the peak disappeared. These findings confirm the synthesis of H̄ atoms in the cusp trap for the first time.
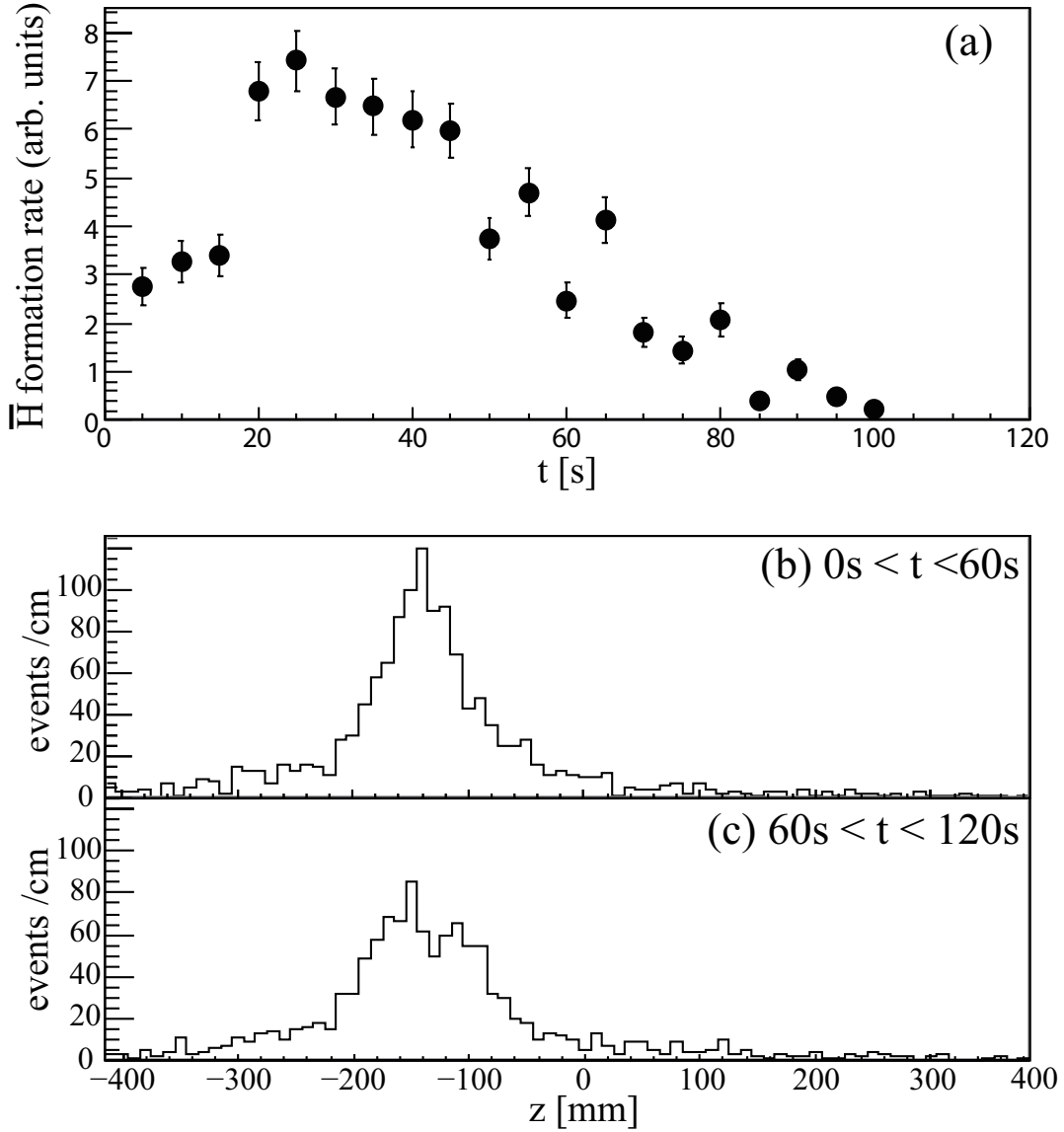
**Figure 7:** *(a) The number of field-ionized H̄ atoms accumulated in FIT monitored by opening the FIT every 5 s. Each data point was obtained repeated the open and close the FIT for 19 times. (b),(c) The annihilation position distributions observed by the 3D detector for 0 s < t < 60 s and 60 s < t < 120 s, respectively.*

Figure 7(a) shows the number of $\bar{p}$s accumulated in FIT every 5 s as a function of time since the start of the mixture of $3 \times 10^5$ $\bar{p}$s in $3 \times 10^6$ $e^+$s. The number increased in the first 30 s and then gradually decreased in the next 80 s yielding totally 70 $\bar{p}$s per mixture. Assuming an isotropic angular distribution of H̄ atoms and taking into account the solid angle covered by the FIT, the total number of H̄ atoms in high Rydberg state was estimated to be about $7 \times 10^3$ per mixture, i.e., the H̄ formation efficiency was about 2% for the above mentioned condition.

We changed the number of $\bar{p}$s for the same number of $e^+$s to see how it makes a difference to the time dependence of the number of field-ionized H̄ atoms. As the number of $\bar{p}$ was decreased (increased), the synthesis rate peaked earlier (later) and the synthesis period became shorter (longer). This observation is consistent with an expectation that the cooling of heated $e^+$s proceeds faster for smaller number of $\bar{p}$s.

We also noticed that the probability of the H̄ synthesis was higher for smaller number of incident p̄s. For example, the H̄ formation efficiency was about 7% for $4 \times 10^4$ p̄s. Figures 7(b) and (c) show p̄ annihilation distribution along the z-axis of the cusp trap obtained by the 3D detector for 0 s< $t$ < 60 s and 60 s< $t$ < 120 s, respectively. A single peak is seen in fig. 7(b) near the $e^+$ trapping position (z = -144 mm). The peak gets broader for fig. 7(c) with an indication of two bumps near the potential maxima of the nested trap (z = -175 mm and z = -113 mm). The latter observation indicates that antiprotons were axially separated from the $e^+$ plasma after several tens of seconds. This axial separation can explain why the H̄ synthesis rate decreased and almost disappeared after 100 s although a large number of p̄s and $e^+$s were still left in the nested trap.
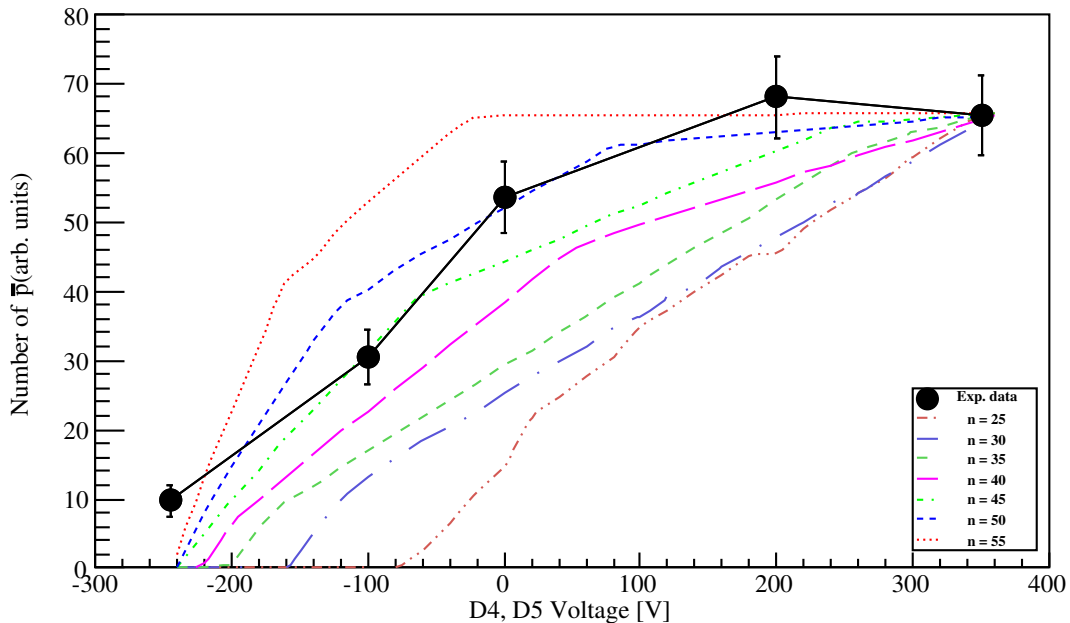


**Figure 8:** *The number of field-ionized H̄ atoms as a function of the voltage applied on the electrodes D4 and D5. The solid circles show the experimental results. Seven curves correspond to field-ionization probabilities are scaled to the experimental value at 350 V.*



**Figure 9:** *Two-dimensional electric field map in cusp trap.*

In order to estimate the principal quantum number $n$ of the field-ionized H̄ atoms, the field strength of the FIT was tuned by changing the voltage $V_{FIT}$ on the electrodes forming the FIT potential. The solid circles in
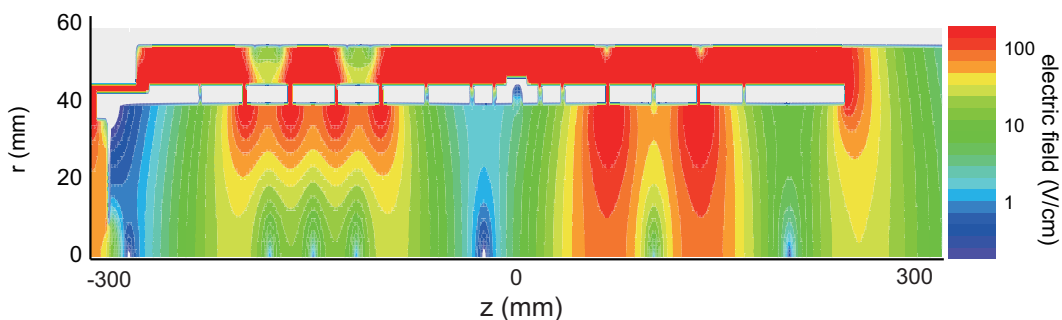
fig. 8 show the number of field-ionized $\bar{\mathrm{H}}$ atoms as a function of the voltage $V_{FIT}$. It is seen that the number of field-ionized $\bar{\mathrm{H}}$ atoms increased as $V_{FIT}$ increased, and then saturated. We calculated the probability for $\bar{\mathrm{H}}$ atoms to be field-ionized and accumulated in the FIT with 2-dimensional map of electric field inside the MRE (see fig. 9), assuming they were drifting out isotropically from the nested well with a specific principal quantum number $n$. We adopted a semi-quantitative formula of field ionization neglecting influence of the magnetic field for the sake of simplicity, $F \sim 3.2 \times 10^8 n^{-4}$(V/m) [7] [10], where $F$ is the minimum field strength at which the atom in the $n$ state is field ionized. Seven curves in fig. 8 show such probabilities for $25 \leq n \leq 55$. The present observation is consistent with the curve for $n \sim$45–50. It is noted that the $\bar{\mathrm{H}}$ atoms with $n \gtrsim 55$ are field ionized by the electric field of the nested trap before they reach the FIT. In the case of three body recombination processes, a typical $n$ can be crudely estimated as $n \sim 400/\sqrt{T(K)}$ by equating the binding energy and the $e^+$ temperature. The temperature of $e^+$ plasma was estimated to be around $1 \times 10^2$ K consistent with a result of our leak mode [11] temperature measurement.

## 1.4    Attempt of $\bar{\mathrm{H}}$ beam extraction from cusp trap

A beam of $\bar{\mathrm{H}}$ is mandatory for the microwave spectroscopy of the ground state hyperfine splitting of $\bar{\mathrm{H}}$ atoms [12]. As already discussed in Ref. [13], the cusp trap provides an axially symmetric minimum $B$ field configuration where low field seeking state (LFS) $\bar{\mathrm{H}}$ atoms are selectively focused whereas high field seeking state (HFS) $\bar{\mathrm{H}}$ atoms are defocused as schematically shown in fig. 10. This results in the formation of a highly spin-polarized $\bar{\mathrm{H}}$ beam. Our preliminary calculation shows that the spin-polarization of a 50 K $\bar{\mathrm{H}}$ beam can be as high as $\sim 30\%$ when they are synthesized near the maximum magnetic field region where we succeeded in synthesizing $\bar{\mathrm{H}}$ atoms in 2010.

We constructed an $\bar{\mathrm{H}}$ detector which consists of a microchannel plate (MCP) and scintillator plates surrounding the MCP. The $\bar{\mathrm{H}}$ detector was located at $\sim$ 1.5 m from nested trap region where solid angle became $1.5 \times 10^{-4}/4\pi$ without assuming the focusing effect by the cusp magnetic field. To distinguish any background such as $\pi^{\pm}$ emitted by annihilation of $\bar{p}$s from the nested trap region or cosmic rays, we monitored the pulse height of each MCP signal. When a low energy $\bar{p}$ hits the MCP and annihilates, a huge energy is deposited on the MCP, which can be easily recognized from the pulse height [14]. By this way, we would distinguish background events from real $\bar{\mathrm{H}}$ events. Although we tried to detect extracted $\bar{\mathrm{H}}$ atoms with this $\bar{\mathrm{H}}$ detector in the last moment in 2010, the beamtime was not enough to confirm the $\bar{\mathrm{H}}$ beam extraction.

## 1.5    Summary of 2010 and plan for 2011

We have succeeded in synthesizing $\bar{\mathrm{H}}$ atoms in the cusp trap, which exclusively enables to extract intensified $\bar{\mathrm{H}}$ beams along the axis. In the present configuration, the formation efficiency from $\bar{p}$s to high Rydberg state $\bar{\mathrm{H}}$ atoms was typically $\sim 2\%$ ($\sim 7\%$ at the maximum in 2010). The time evolution of $\bar{\mathrm{H}}$ formation rate was also studied with the field-ionization technique.

We finalized the design of a 1.42-GHz radiofrequency resonator in 2010, and started construction at CERN. The major parts have already been manufactured, and only a few smaller pieces still need to be manufactured or ordered. Inside the resonator, a weak, homogeneous static magnetic field needs to be present, therefore the strong stray magnetic field of the cusp trap at the position of the resonator needs to be decreased. A design of a magnetic shielding has been started, but it turned out to be much more complicated than expected, therefore most likely only the first component of the magnetic shielding will be installed in 2011. A superconducting sextupole magnet, which acts as a spin analyzer focusing or defocusing the atoms onto the antihydrogen detector depending on their spin direction, will soon be tested and commissioned, so that it is ready for the beam time in 2011.
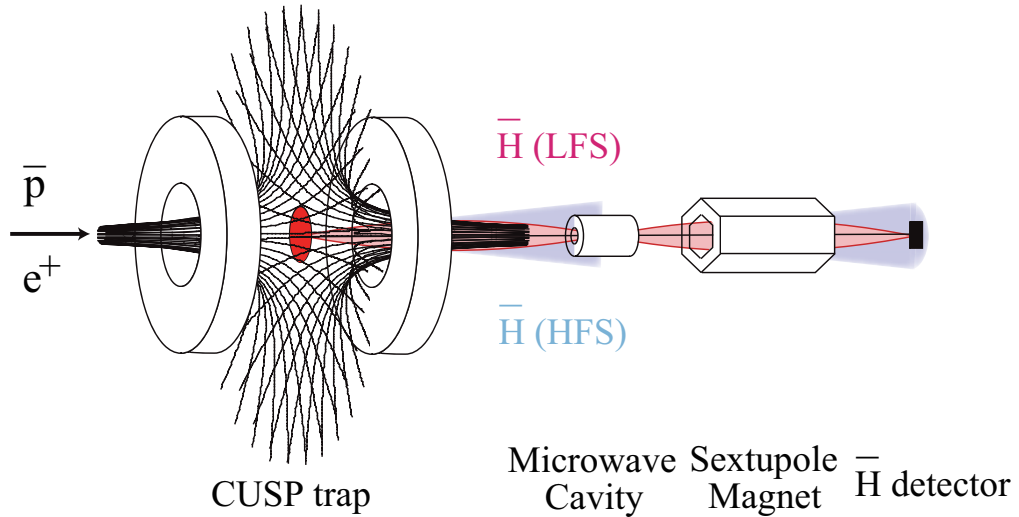
**Figure 10:** *A conceptual experimental setup for the ground-state hyperfine transition measurement of H̄ atoms with the cusp trap.*

In 2011, the cusp trap experiment will be performed in two steps. In the first step, we will keep the experimental setup as used in 2010, and optimize the H̄ beam extraction conditions with respect to $\bar{p}$ and $e^+$ temperatures, the number and density of $\bar{p}$s and $e^+$s, $\bar{p}$ injection energies, the shape of the nested trap potential, *etc*. In the second step after optimization, the microwave cavity and the sextupole magnet will be installed between the cusp trap and the H̄ detector (see fig. 10), which allows us to start the microwave spectroscopy of the ground state hyperfine transitions of H̄ atoms [12,15] similar to the ones which were used in the early days of hydrogen HFS spectroscopy. The oscillating magnetic field in the resonator can flip the spin of the H̄ atoms when it is on resonance with one of the hyperfine transitions. Although the spectroscopic results would be preliminary even if successful, it would then be the real first transition measurement on H̄ atoms. All the necessary components to make the microwave spectroscopy such as the cavity and the sextupole magnet are almost ready.

We are also going to improve the 3D detector performance before the beamtime in 2011. In particular, we plan:

- to optimize the coupling between fibers and Hamamatsu multianode PMTs, with the possibility to improve by a factor of two or three the vertex reconstruction efficiency. We are currently developing a method to test the coupling efficiency;

- to renew the electronics readout, which makes it possible to reconstruct annihilation positions also for a pulse-extraction antiprotons from the field ionization trap (FIT);

- to firmly fix the four modules of the 3D detector mechanically for the best alignement and positioning;

- to be able to get triggers from different scintillator layers.

## 2 Development of a superconducting radiofrequency Paul trap for antiprotons

In 2010 the ASACUSA collaboration, together with support from the CERN AB division completed the 3-m-high cryostat and cryogenic cooling system needed to cool the Paul trap to temperature $T \sim 1.5$ K. The

cryostat was successfully tested over a period of 2 weeks at the CERN cryolab. The cavity, vacuum parts, and sapphire support structures of the Paul trap have been constructed, and we are finishing the manufacturing and welding of the trap structure itself for testing in 2011–2012.

# 3  First laser-spectroscopy of ultra-cold antiprotonic helium atoms

In 2010, we succeeded to cool $\overline{p}\mathrm{He}^+$ atoms to temperature $T \sim 1.5$ K by employing the technique of gas buffer cooling in dilute helium gas, and carried out parts-per-billion-scale, single-photon laser spectroscopy experiments on these ultra-cold atoms for the first time. This is nearly an order of magnitude colder than the atoms used in our recent experimental results of Ref. [16]. We measured seven transitions in the $\overline{p}{}^4\mathrm{He}^+$ and $\overline{p}{}^3\mathrm{He}^+$ isotopes, which in previous experiments [16] showed differences of 1–3 parts in $10^8$ compared to the results $v_{\mathrm{th}}$ of three-body QED calculations [17]. Due to the much lower temperature and the improved laser systems used in 2010, both the experimental precision and the experiment-theory difference was reduced to 5–6 parts in $10^9$. When extended to other laser transitions which are planned to be measured in 2011, these experiments may lead to the most precise comparison of the antiproton and proton charges and masses so far carried out by $\overline{p}\mathrm{He}^+$ spectroscopy.

The production of cold atoms is essential for improving the experimental precision of laser spectroscopy for several reasons, i): *reduction of thermal Doppler broadening*, the thermal motion of the atoms in the target broadens the full-width at half maximum (FWHM) linewidth of the measured resonance lines to,

$$\Delta v_D = 2.35 v \sqrt{\frac{kT}{Mc^2}}, \tag{1}$$

wherein $M$ and $T$ denote the mass and temperature of the atom, $k$ the Boltzmann constant, and $c$ the speed of light. The resulting uncertainty in the determination of the resonance centroid imposes a fundamental limit on the experimental precision. The above equation implies, however, that a 1/10 reduction of $T$ results in a narrowing of the resonance line by factor $< 1/3$, ii): *increase of signal-to-noise ratio*, since at low temperature more atoms are distributed in a narrow thermal distribution, the signal intensity would correspondingly increase, iii): *reduction of collisional relaxation*, high rates of atomic collisions between $\overline{p}\mathrm{He}^+$ and normal helium atoms in the experimental target can cause unwanted shortening of the atom's lifetime against annihilation, due to a variety of collisional cascade processes that can cause rapid absorption of the antiproton in the helium nucleus. At low temperature, the rate of these collisions decreases with $\sqrt{T}$.

The cooling was accomplished by allowing the $\overline{p}\mathrm{He}^+$ atoms to collide with normal helium atoms in a gas target maintained at temperature $T = 1.5$–1.6 K and pressure $P \sim 0.5$–2 mbar. Prior to this experiment, it was unclear whether the $\overline{p}\mathrm{He}^+$ would really cool to such temperatures simply by atomic collisions. Indeed, in some exotic atoms these collisional deexcitations can result in the recoil and heating of the atom by chemical processes. For this experiment we constructed a new 3-m-high cryogenic helium target and cryocooler pumping system. Antiprotons of energy 5.3 MeV extracted from the AD were first decelerated to 80 keV using the radiofrequency quadrupole decelerator (RFQD). This beam was transported by an achromatic magnetic beamline to the position of the cryogenic gas target. The target chamber was machined out from a solid piece of $150 \times 150 \times 150$ mm oxygen-free high conductivity (OFHC) copper. The resonant laser beam entered through a fused silica window fixed on one side of the target at Brewster's angle, and exited though a second window on the opposite side. This chamber was connected to a cryogenic cooler (Fig. 11) which consisted of a 1.5-K helium pot, a superfluid helium heat exchanger, several cryogenic needle valves, and a 150-mm-diameter pumping line. The pumping line was connected to a roots blower of pumping speed 2000 $\mathrm{m}^3$/h and rotary vane pump of 700 $\mathrm{m}^3$/h. Liquid helium was allowed to pass through the heat exchanger and expand through a needle valve into the 1.5-K pot maintained at a pressure of a few mbar. This Joule-Thompson expansion cooled the helium to 1.5 K, allowing a superfluid film to develop on the inner walls
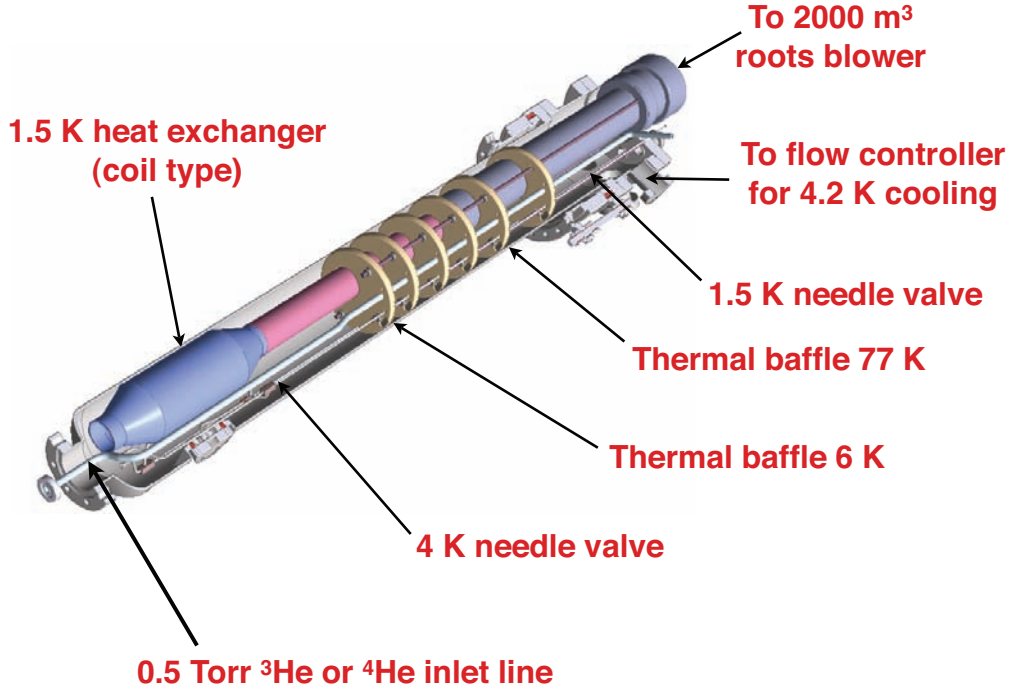
**To 2000 m³ roots blower**

**1.5 K heat exchanger (coil type)**

**To flow controller for 4.2 K cooling**

**1.5 K needle valve**

**Thermal baffle 77 K**

**Thermal baffle 6 K**

**4 K needle valve**

**0.5 Torr ³He or ⁴He inlet line**

**Figure 11:** *Schematic drawing of cryocooler used to cool $\overline{p}He^+$ atoms to temperature $T = 1.5$ K.*

of the pot to which the copper target chamber was thermally anchored. Despite the large thermal radiation entering through three 50-mm-diam windows into the target, the chamber was maintained at $T = 1.5$ K for up to 10 h.
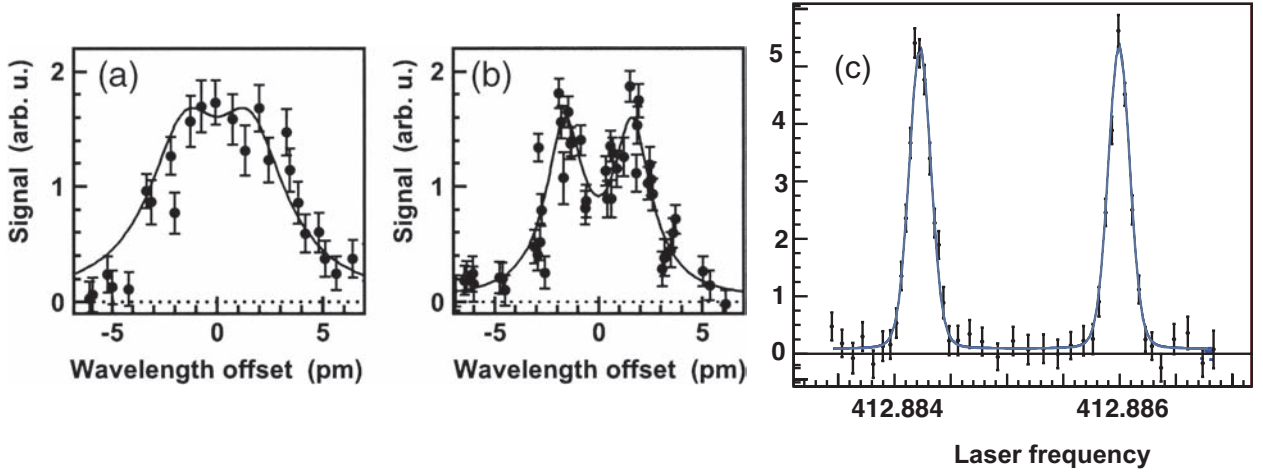


**Figure 12:** *Laser resonance $(n, \ell) = (37, 35) \rightarrow (38, 34)$ in $\overline{p}^4He^+$ measured in 2000 by ASACUSA collaboration (a) and measured using a 100-keV antiproton beam decelerated by RFQD (b). Resonance measured in 2010 using atoms cooled to 1.5 K and pulsed Ti:Sapphire laser (c), note factor 10 improvement of spectral resolution.*

Fig. 12 (c) shows the profile of the transition $(n, \ell) = (37, 35) \rightarrow (38, 34)$ of $\overline{p}^4He^+$ atoms cooled to $T \sim$ 1.5 K which we measured in 2010. We used a narrowband Ti:Sapphire laser developed by the ASACUSA

collaboration [18], which has among the smallest linewidths ($\sim 6$ MHz) for a nanosecond laser with high output energy $E = 50$–$100$ mJ. The two peaks seen here are the hyperfine structure which arises from the dominant interaction between the orbital angular momentum of the antiproton and the electron spin. The spectral resolution is an order of magnitude higher compared to previous experiments [Figs. 12 (a) and (b)] carried out on hotter atoms $T \sim 10$ K and using an organic dye laser of larger spectral linewidth. The statistical fluctuation in the new data of 2010 [Fig. 12 (c)] are also smaller due to the greater numbers of $\overline{p}\text{He}^+$ atoms that lie within the region of the thermal distribution excited by the laser beam.
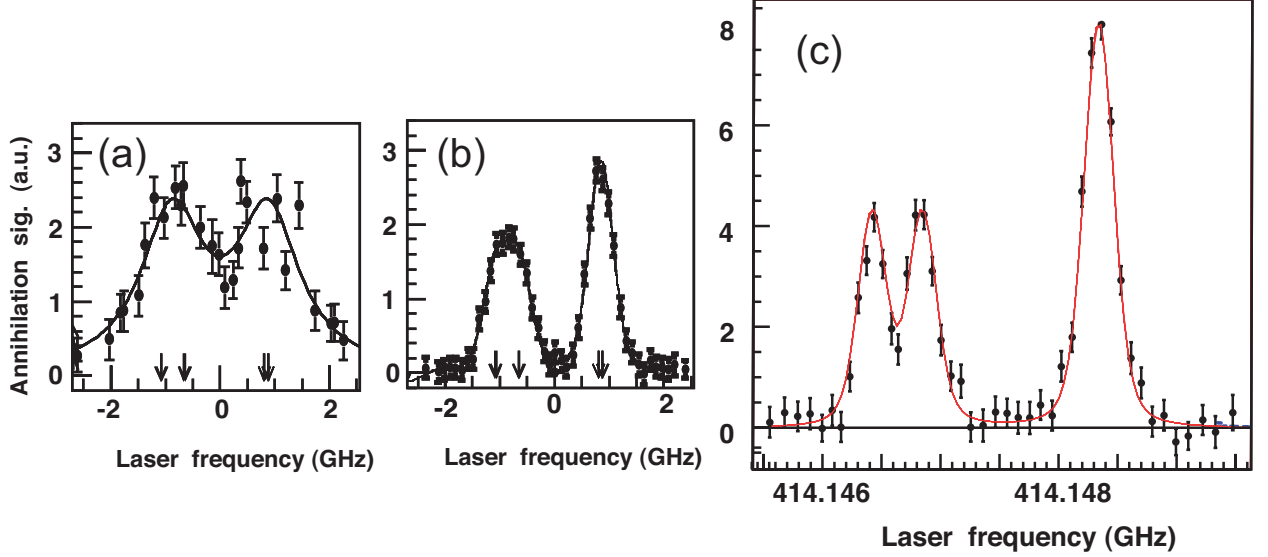


**Figure 13:** *Laser resonance* $(n, \ell) = (36, 34) \rightarrow (37, 33)$ *in* $\overline{p}^3\text{He}^+$ *measured using the highest-resolution commercial pulsed laser (a), and using a cw-pulse amplified dye laser developed by ASACUSA (b). The two-peak structure is due to the dominant interaction between the orbital angular momentum of the antiproton and the electron spin. Atoms cooled to 1.5 K together with the pulsed Ti:Sapphire laser used in 2010 (c) resulted in an even higher spectral resolution. The three-peak structure resolved here for the first time is due to the additional interaction between the nuclear spin of* $^3\text{He}$ *and the electron.*

Fig. 13 (c) shows the profile of the resonance $(n, \ell) = (36, 34) \rightarrow (37, 33)$ in $\overline{p}^3\text{He}^+$ cooled to $T \sim 1.5$ K. As in the $\overline{p}^4\text{He}^+$ case, the spectral resolution is much higher than in previous experiments [Fig. 13 (a)–(b)] at $T > 10$ K. We resolved a three-peak structure due to the additional interaction between the nuclear spin of $^3\text{He}$ and the electron.

We next examined how the measured frequencies $\nu_{\text{exp}}$ of 2010 related to past measurements. Fig. 14 shows the deviations of the experimental (circles with $1\sigma$ errors) and calculated [17] frequencies ($\nu_{\text{th}} - \nu_{\text{exp}})/\nu_{\text{exp}}$ published in 2006. For the four highest-precision measurements in $\overline{p}^4\text{He}^+$ and $(n, \ell) = (36, 34) \rightarrow (37, 33)$ in $\overline{p}^3\text{He}^+$ the agreement was better than 10 parts per billion. Four of experimental $\overline{p}^3\text{He}^+$ frequencies, however, were 30–40 parts per billion below the theoretical values. To further improve the precision on $m_e/m_{\overline{p}}$, it was vital to study the possible reasons for this 2-$\sigma$ difference between $\nu_{\text{exp}}$ and $\nu_{\text{th}}$ Fig. 14. Theoretical studies [19] carried out in 2008–2009 revealed a possible source of systematic shift in $\nu_{\text{exp}}$. In Ref. [16], the $\overline{p}\text{He}^+$ atoms were synthesized by allowing antiprotons to enter a 150-mm-diameter, 300-mm-long stainless steel chamber filled with helium gas of temperature $T \sim 10$–$12$ K. The pulsed laser beam intercepted the antiprotons in an anticollinear geometry. This caused part of the laser beam to reflect or scatter off the stainless steel walls and flanges of the target, so that the $\overline{p}\text{He}^+$ were simultaneously irradiated by laser light from several directions. Different parts of the atom's thermal distribution were depopulated simultaneously,
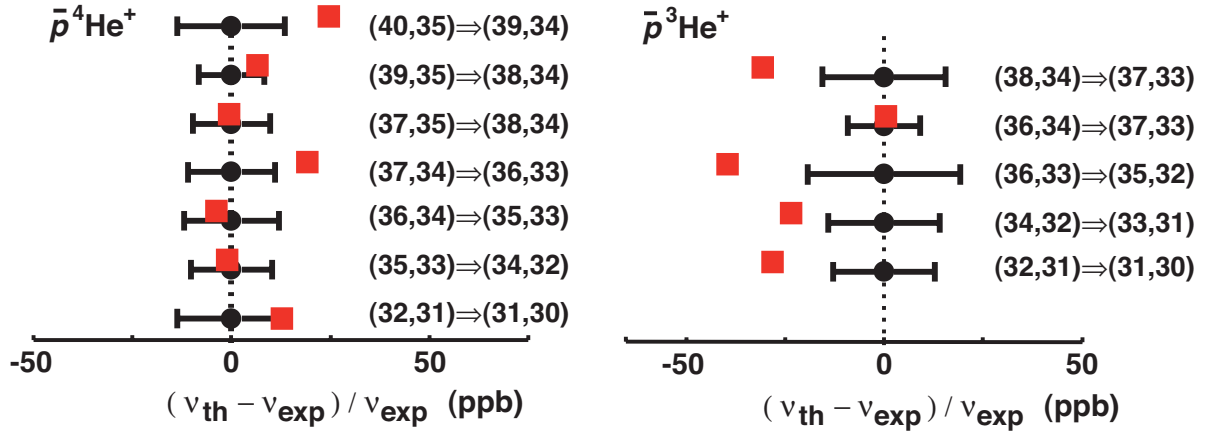
**Figure 14:** *Experimental $\nu_{exp}$ (circles with $1\sigma$ errors) [16] vs theoretical $\nu_{th}$ [17] transition frequencies used in 2006 to determine the antiproton-to-electron mass ratio. For the four highest-precision measurements in $\overline{p}^4\text{He}^+$, and $(n, \ell) = (36, 34) \rightarrow (37, 33)$ in $\overline{p}^3\text{He}^+$ the agreement was better than 10 parts per billion. Four of experimental $\overline{p}^3\text{He}^+$ frequencies, however, were $\sim 2\sigma$ below the calculated ones corresponding to 30–40 parts per billion.*

so that under certain conditions, the resonance profile can become skewed. This effect appears stronger in $\overline{p}^3\text{He}^+$ due to its complicated hyperfine structure consisting of eight sublines [19] arising from the spin interactions between the three constituent particles. The spacings between these sublines are highly asymmetric as shown in Fig. 13. By comparison, $\overline{p}^4\text{He}^+$ has four hyperfine sublines which are relatively symmetrically spaced [Fig. 12].

The lower $\overline{p}\text{He}^+$ temperature reduced these systematic errors associated with the Doppler broadening, whereas the resolution was increased by a factor 3–4. In addition, the laser intersected the antiproton beam at a 90-degree angle before leaving the target through another window, which eliminated the problems with scattering of the laser beam. Seven transitions $(37, 35) \rightarrow (38, 34)$, $(37, 34) \rightarrow (36, 33)$, $(34, 33) \rightarrow (35, 32)$, $(35, 33) \rightarrow (34, 32)$ in $\overline{p}^4\text{He}^+$, and $(36, 34) \rightarrow (37, 33)$, $(36, 33) \rightarrow (35, 32)$, $(34, 32) \rightarrow (33, 31)$ in $\overline{p}^3\text{He}^+$ were measured with a precision of 5–15 parts in $10^9$. The experiment-theory difference was $< 6 \times 10^{-9}$ for many of the transitions which constitutes an improvement of a factor $\sim 4$ for many of these lines.

## 3.1 Plans for 2011: Completion of single-photon laser spectroscopy experiments on cold $\overline{p}\text{He}^+$ atoms

Before we can complete these high-precision experiments of the single-photon transition frequencies of $\overline{p}\text{He}^+$ relevant to our CPT consistency tests, we must extend the measurements to all 12–14 transitions as in our previous generation of measurements published in 2006. This would allow a through study of the systematic deviations of the experimental transition frequencies over a wide range of principle and angular momentum quantum numbers. These resonances have different radiative and Auger widths, hyperfine splittings, absorption wavelengths, and sensitivities to the antiproton mass and charge, and so it is important to measure all of them in a systematic way. We plan to therefore measure the remaining 5–7 transitions in $\overline{p}^4\text{He}^+$ and $\overline{p}^3\text{He}^+$ in 2011.

# 4 Spectroscopy of the Hyperfine Structure of Antiprotonic Helium

A precise measurement of the antiprotonic helium ($\overline{p}He^+$) [26–29] *hyperfine structure* (HFS) can be compared with three-body Quantum Electrodynamic (QED) calculations [30, 31] as a test of their predictions. If the theoretical and experimental values agree within their errors, a comparison between the measured transition frequencies and three body QED can be used to determine the antiproton spin magnetic moment and thus lead to a test of CPT invariance. The HFS of the $(n,l) = (37,35)$ state of $\overline{p}^4He^+$ has now been thoroughly measured [32, 33]. The precision achieved for the $(n,l) = (37,35)$ state in $\overline{p}^4He^+$ cannot be improved anymore due to fluctuations of the $\overline{p}$ beam. Therefore, a first measurement of $\overline{p}^3He^+$ was proposed which can be performed with a similar experimental setup. We have received FWF[1] funding (proposal number I-198-N20) for this three year project. In 2009, the measurement of a new state has been started: the $(n,l) = (36,34)$ state of $\overline{p}^3He^+$. The measurement of this state is the first hyperfine structure measurement in $\overline{p}^3He^+$. $\overline{p}^3He^+$ is a more complex system than $\overline{p}^4He^+$ as described below. A comparison between the theoretical calculations and experimental results would lead to a more rigorous test of the theory. Additionally it would address a $2\sigma$ deviation between the theoretical calculations and laser transitions measured in 2006 [34]. This year, we could observe a signal for two out of four allowed SSHF transitions. A publication in Physics Letters B is currently in progress on the first successful observation of SSHF transition lines in $\overline{p}^3He^+$. It is planned for 2011 to measure all four SSHF lines, two at 11 GHz and two at 16 GHz.
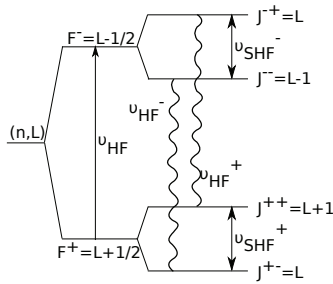


**Figure 15:** *Hyperfine splitting (HFS) of a state $(n,l)$ of $\overline{p}^4He^+$. The wavy lines denote allowed M1 transitions that can be stimulated by microwave radiation.*
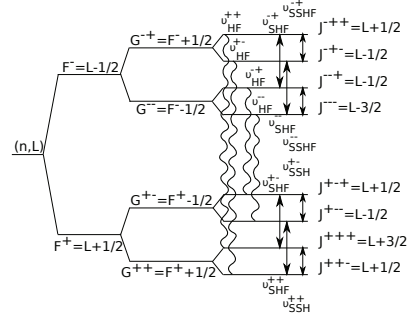
**Figure 16:** *Hyperfine splitting (HFS) of a state $(n,l)$ of $\overline{p}^3He^+$. The wavy lines denote allowed M1 transitions that can be stimulated by microwave radiation.*

The HFS of $\overline{p}He^+$ arises from the interaction of the magnetic moments of its constituents and has been calculated by Korobov and Bakalov to $\alpha^4$ order [30, 31]. For the electron spin-orbit interaction term of the $(n,l) = (35,37)$ state in $\overline{p}^4He^+$ also the higher order correction $m\alpha^6$ has been calculated [35]. They constructed an effective Hamiltonian for $\overline{p}^4He^+$

$$H^{\text{eff}} = E_1(\vec{L}\cdot\vec{S}_e) + E_2(\vec{L}\cdot\vec{S}_{\overline{p}}) + E_3(\vec{S}_e\cdot\vec{S}_{\overline{p}})$$

$$+ E_4\{2L(L+1)(\vec{S}_e\cdot\vec{S}_{\overline{p}}) - 6[(\vec{L}\cdot\vec{S}_e)(\vec{L}\cdot\vec{S}_{\overline{p}})]\}. \tag{2}$$

Due to the large orbital angular moment of the antiproton ($\vec{L} \sim 35$), the dominant splitting arises from the interaction of $\sim \vec{L}$ with the electron spin $\vec{S}_e$. The antiproton spin $\vec{S}_{\overline{p}}$ and the spin $\vec{S}_h$ of the 'helion' h, the $^3$He nucleus, lead to further splittings leading to a quadruplet for $\overline{p}^4He^+$ and an octet for $\overline{p}^3He^+$. The effective Hamiltonian for $\overline{p}^3He^+$ is more complicated and contains nine terms [36].

In Fig. 15 and Fig. 16 the allowed M1 transitions that can be induced by an oscillating magnetic field are shown. In the case of $\overline{p}^4He^+$, there are two types of transitions: HF transitions ($v_{\text{HF}}^+$ and $v_{\text{HF}}^-$) which are

14

associated with a spin-flip of the electron, and *superhyperfine (SHF)* transitions ($v_{\text{SHF}}^{+}$ and $v_{\text{SHF}}^{-}$) which are associated with a spin flip of the antiproton.

In the case of $\bar{\text{p}}^3\text{He}^+$, there is an additional transition. The HF transitions are still associated with the spin flip of the electron ($v_{\text{HF}}^{++}$, $v_{\text{HF}}^{+-}$, $v_{\text{HF}}^{-+}$ and $v_{\text{HF}}^{--}$). Although the helion magnetic moment is smaller than that of the antiproton, its overlap with the electron cloud (which is in the ground state and has its maximum probability at the helion site) is stronger. Therefore the helion spin contributes to the quadruplet superhyperfine splitting ($v_{\text{SHF}}^{-+}$, $v_{\text{SHF}}^{--}$, $v_{\text{SHF}}^{+-}$ and $v_{\text{SHF}}^{++}$) and *super-superhyperfine (SSHF)* transitions are caused by the spin flip of the antiproton ($v_{\text{SSHF}}^{-+}$, $v_{\text{SSHF}}^{--}$, $v_{\text{SSHF}}^{+-}$ and $v_{\text{SSHF}}^{++}$) [28].

The transitions between the SSHF octets of $\bar{\text{p}}^3\text{He}^+$ can be measured with the same method as those between the SHF quadruplets of $\bar{\text{p}}^4\text{He}^+$. Instead of two transitions, shown in Fig. 15), there are now four as shown in Fig. 16). The most appropriate candidate state is the $(n,l) = (36,34)$ state, which has an unfavoured laser transition to (37, 33) of $\sim$723 nm, close to that of the previous measurement ($\sim$726 nm) and of similar intensity. Korobov and Bakalov calculate the microwave transitions as the following [36]:

**11 GHz transitions:**

$$J^{+-+} = L + \frac{1}{2} \mapsto J^{--+} = L - \frac{1}{2} = 11.1250\,\text{GHz} \tag{3}$$

$$J^{+--} = L - \frac{1}{2} \mapsto J^{---} = L - \frac{3}{2} = 11.1577\,\text{GHz} \tag{4}$$

Difference = 32.73 MHz

**16 GHz transitions:**

$$J^{+++} = L + \frac{3}{2} \mapsto J^{-++} = L + \frac{1}{2} = 16.1107\,\text{GHz} \tag{5}$$

$$J^{++-} = L + \frac{1}{2} \mapsto J^{-+-} = L - \frac{1}{2} = 16.1434\,\text{GHz} \tag{6}$$

Difference = 32.72 MHz

## 4.1 Experimental Method

The laser spectroscopy method (see Fig. 17) takes advantage of the charged pions produced when the antiproton annihilates in the helium nucleus. An exponentially decaying background signal is ever present as the antiprotons, in various levels of the cascade, decay and eventually annihilate in the nucleus. This is referred to as an *analog delayed annihilation time spectrum (ADATS)*, analog because a voltage proportional to the number of events is recorded. A measurement of a particular state can be made by laser stimulated transfer to a fast-decaying, Auger decay dominated, daughter state. The ratio of the peak area to the total background area (peak-to-total) indicates the size of the population transferred from the parent to the daughter state.

A microwave pulse can be used to transfer the populations between SSHFS octet states via an electron spin flip. Combined with the laser, to make a laser-microwave-laser technique, this method can be used to measure the transition frequencies.

Initially all the octet states are equally populated and so a population asymmetry must first be induced. A narrow band laser pulse, tuned to the $f^+$ transition, creates this asymmetry. The $J^{+-+}$, $J^{+--}$, $J^{+++}$ and $J^{++-}$ octet states are depopulated through a laser induced transfer to the Auger dominated decay state, while the $J^{-++}$, $J^{-+-}$, $J^{--+}$ and $J^{---}$ octet states remain relatively unaffected. This produces the first peak shown in Fig. 18. The microwave envelope follows which, if on resonance, results in partially inverting the
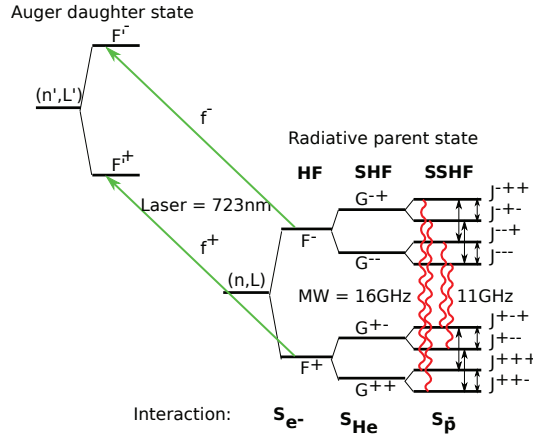
**Figure 17:** *Schematic drawing of the laser-microwave-laser method. Dashed arrows indicate the laser transitions between HF levels. Wavy lines illustrate the microwave-induced transitions between the SSHF levels of the radiative decay state.*
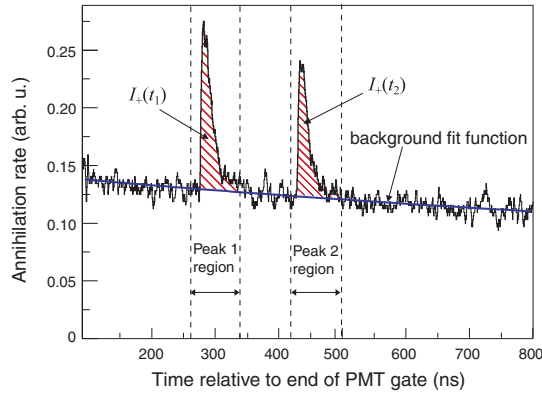


**Figure 18:** *Two laser stimulated annihilation peaks against the exponential decaying background of the other state populations. The peak-to-total of each is calculated by taking the ratio of the peak area ($I_+$) to the total area under the full spectrum.*

asymmetry: refilling either the $J^{+--}$ or $J^{+--}$ from the $J^{--+}$ or $J^{---}$ octet state in the $\sim$11 GHz region or the $J^{+++}$ or $J^{++-}$ from the $J^{-++}$ or $J^{-+-}$ octet state in the $\sim$16 GHz region respectively. After refilling, a second laser pulse, tuned to the same $f^+$ transition, is used to depopulate the doublet state again, producing the second peak shown in Fig. 18.

The first laser-induced annihilation peak remains constant, fluctuating only statistically or with the varying conditions of the target, and is therefore used to normalise the second. The second annihilation peak corresponds directly to the population transferred between the hyperfine substates by the microwave. The microwave frequency is scanned across the expected resonant frequency. A plot of the microwave frequency vs the normalised second annihilation peak, produces a peak at the resonant frequency.

## 4.2  Experimental Apparatus

The principle of the new experiment with $\overline{p}^3He^+$ is the same as that for the $\overline{p}^4He^+$ $(n,l) = (37,35)$ state measurements. Therefore the required apparatus essentially remained the same. The microwave setup is described in detail by Sakaguchi *et al.* [37] while the laser system is described in Hori *et al.* [34] and summarised in Pask *et al.* [33]. The laser transition between the parent state $(n,l) = (36,34)$ and the Auger
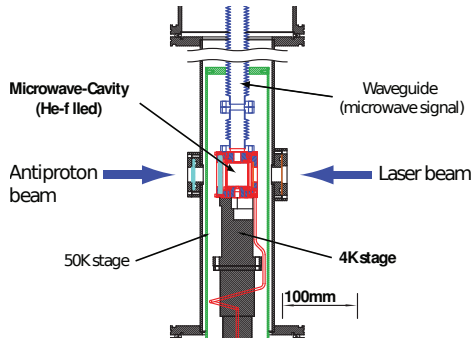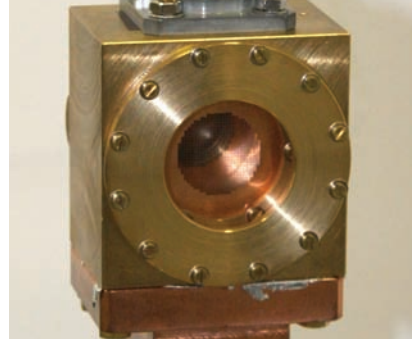
**Figure 19:** *A drawing of the new cryostat*



**Figure 20:** *A photograph of the new cavity, mounted on the coldhead*

decay dominated state $(n,l) = (37,33)$ is $\sim$723 nm so an identical laser system can be used. A new cavity for the 11 GHz transitions and a new cryostat with a compressor-based cooling system have been designed and built in Vienna, see Fig. 19 and Fig. 20. Further a new microwave signal generator and amplifier are in use. To produce a 16 GHz microwave signal will further require new waveguides and another cavity.
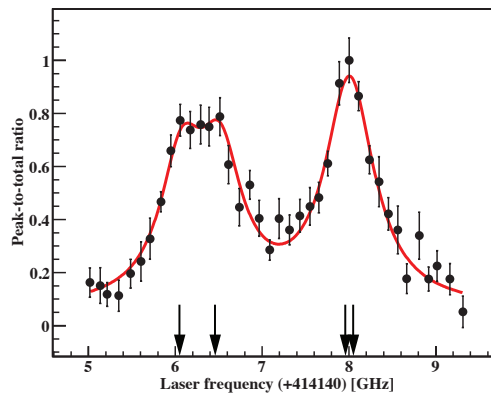
## 4.3  2010 Measurements



**Figure 21:** *Laser resonance profile for $\bar{p}^3He^+$, displaying the two laser transitions $f^+$ and $f^-$. The peaks are fitted with four Lorentzian functions corresponding to the four allowed E1 transitions). The arrows indicate the theoretical transition frequencies.*

This beamtime was split up in two parts. We started with the measurement of the $(n,l) = (37,35)$ state in $\bar{p}^4He^+$ which has already been well investigated. After the beamtime of 2009 when we measured with $\bar{p}^3He^+$ for the first time, we optimized the microwave diagnostics to obtain a more reliable characterization of the microwave cavity in terms of field mode, field magnitude and eigenresonance frequency. Thus, now a verification of the measurement of the $(n,l) = (37,35)$ state in $\bar{p}^4He^+$ with the new experimental design confirmed the proper working of the setup. Also, the new cryostat (see Fig. 19) worked successfully. It could be kept very stable at a pressure of $\sim$250 mbar and the cavity temperature stabilized within minutes. In the course of this, we were further able to finish a study on collisional relaxations which could not yet be completed due to insufficient statistics. These measurements required to build a new cavity, which could be mounted within the new cryostat.

In the second part we measured the $(n, l) = (36, 34)$ state of $\bar{p}^3He^+$ transitions at 11 GHz with a new microwave cavity. Two of the four favoured SSHF resonance lines in $\bar{p}^3He^+$ could be observed. A scan over the laser frequency range was done to determine the frequency offset and the splitting of the two HF lines (see Fig. 21) to ensure that only one of the two hyperfine levels of the $(n, l) = (36, 34)$ state is depopulated by laser stimulation. The splitting is $\Delta f = 1.714 \pm 0.025$ GHz, similar to the transition at ~726 nm in $\bar{p}^4He^+$. Due to the different SSHF energy level spacings one of the laser transition peaks has a lower amplitude and larger width. Two of the four SHF energy levels are lying so close to each other to have a splitting smaller than the laser linewidth and Doppler width of 100 MHz and 300 MHz and can thus not be resolved while the other two SHF lines should be visible as distinct peaks.

The measured hyperfine transitions agree with theory within 1 MHz. The results of the two microwave-induced transitions between SSHF states in $\bar{p}^3He^+$ are displayed in Fig. 22. They were both fitted with the function of their natural line shape. From the fit one obtains the frequencies for the measured $\nu_{HF}^{--}$ and $\nu_{HF}^{-+}$ transition.

Even though the current precision of ~20 ppm is still less than for the most recent results with $\bar{p}^4He^+$ which gave an error of 3 ppm for the individual transition lines [38], the results roughly agree with the theoretical predictions. Due to limitations in antiproton beam quality this precision for $\bar{p}^4He^+$ can not be improved anymore. However, it is also unlikely to achieve an error for $\bar{p}^3He^+$ as small as for $\bar{p}^4He^+$. There are eight instead of four SSHF energy levels in $\bar{p}^4He^+$ and thus the measured signal will be only about half of the signal obtained for $\bar{p}^4He^+$. Therefore, much higher statistics would be required. A comparison of the theoretical values for the two SSHF transitions at 11 GHz to the measurement results shows that there is a small shift in frequency towards higher values for both transitions. The frequency difference $\Delta\nu_{\text{th-exp}}$ between theory and experiment is ~0.6 MHz for $\nu_{HF}^{--}$ and ~0.7 MHz for $\nu_{HF}^{-+}$ respectively. According to V. Korobov, this discrepancy is most likely due to the theoretical limits of the Breit-Pauli approximation that has been used for the calculations. The relative error is estimated to be $\alpha^2 = 5 \times 10^{-5}$. The theoretical error for the frequency difference would then be ~0.6 MHz. Together with the experimental error of ~0.2 MHz there is agreement between experiment and theory. Higher order correction terms need to be calculated to improve the theoretical results. The work on these calculations is in progress [39]. The precision of the theoretical value for the frequency difference $\Delta\nu_{HF}^{\pm} = \nu_{HF}^{-+} - \nu_{HF}^{--}$ between the two SSHF lines at 11 GHz instead is considerably higher, i.e. 1.6 MHz, than for the frequency difference obtained from the measured transitions.

The electric dipole moments of the $(36, 34) \rightarrow (37, 33)$ transition in $\bar{p}^3He^+$ are of the same order as those of the measured transition in $\bar{p}^4He^+$ and it has been shown that the two hyperfine transitions can be well resolved [34]. However the presence of twice as many states increases the microwave resonant profile background and therefore reduces the relative signal, according to preliminary simulations to about 10-15%. Therefore, the measurements are very sensitive to fluctuations of the antiproton or the laser beam and it is crucial to accumulate enough statistics to see a significant, reproducible signal. Even though the provided antiproton intensity was good this year, it took more than a week to properly tune the beam within the ASACUSA beamline. About 25% of our beamtime there were no antiprotons available in the AD at all.

## 4.4 Proposed Measurements for 2011 and Beamtime Request

We are planning to measure all four allowed SSHF transitions of the $(n, l) = (36, 34)$ state in $\bar{p}^3He^+$. Since there are two pairs of transitions lying close to each other, at 11 GHz and at 16 GHz, the microwave cavity needs to be changed during the beamtime. The two transitions at 11 GHz have already been observed in 2010. Therefore, we will start with these two SSHF lines to gain sufficient statistics. A higher precision of the single transition lines is particularly important in order to reduce the error of the frequency difference of the transitions. The theoretical precision for this value is still considerably higher than for the measurement. The microwave power dependence has to be checked again thoroughly in order to optimize the signal-
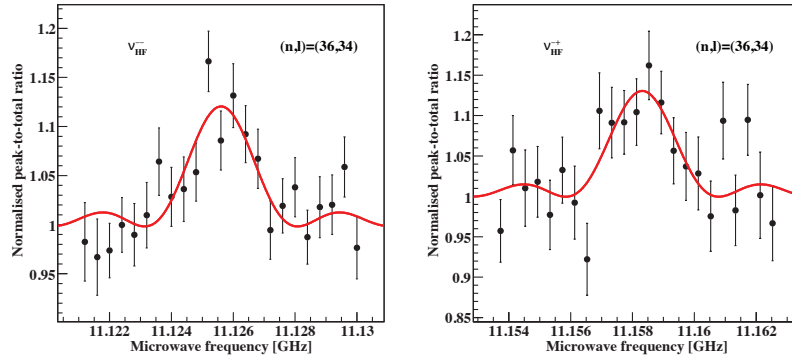
**Figure 22:** *Scan over the microwave frequency for two of the four SSHF transitions in $\bar{p}^3He^+$, each fitted with the natural line shape. The frequencies of the measured transitions are $11.12559 \pm 0.00014$ GHz and $11.15839 \pm 0.00018$ GHz. The transition frequencies are predicted by theoretical calculations [36].*

to-noise ratio. We further aim to do all measurements at different target densities. This is necessary to determine the results at zero density in particular to be sure that no density shift exists, as predicted by theory [40].

The 16 GHz transitions will be measured for the first time. Thus, it will be important to study the microwave signal, obtained from the laser annihilation rate(s) and the microwave power, i.e. the magnetic field strength inside the cavity, with good enough statistics to confirm simulations. The goal will be to observe all four allowed transition lines and complete the measurement of the hyperfine structure of this $\bar{p}^3He^+$ state. The 16 GHz transitions are planned to be studied only at one target density.

Due to the limited amount of available beamtime for this experiment, it will be necessary to postpone a thorough study of density effects and the accumulation of sufficient statistics in particular for the 16 GHz transitions to 2012. This will not be feasible in 2011.

# 5  Ionization of atoms and molecules by slow antiprotons

## 5.1  Progress during 2010

During our run in 2010 we were able to measure the cross section for single, non-dissociative ionization of molecular hydrogen for antiproton impact in the energy range $2 - 11$ keV [20]. These data constitute an extension of our recent measurements of single ionization cross sections for helium and argon [21, 22] to molecular targets, and – as discussed below – reveals a new mechanism which largely determines the cross section at low energy antiproton impact on molecules.

Figure 23 shows our new experimental results for molecular hydrogen (from ref [20]) compared with a solid curve which indicates the behaviour of the cross section for single ionization of atomic hydrogen. It is calculated from a simple "Effective Fermi-Teller" model which uses a calculation of the binding of the electron in a static system of a hydrogen atom and an antiproton at distance R from the proton. Such a calculation gives a distance where the electron becomes unbound of $R_{FT} = 0.639a_0$ or a cross section of $\pi R_{FT}^2 = 0.35\mathring{A}^2$. However, since our collisions, albeit being slow, are not adiabatic, we take into account the broadening of the binding energy $\delta(E)$ due to the duration of the collision $\delta(t)$, using $\delta(E)\delta(t) = \hbar$. This gives an effective release distance $r_{eff}$. We also introduce a multiplicative "release probability" $P_{release}$, which for atomic targets is 0.5:

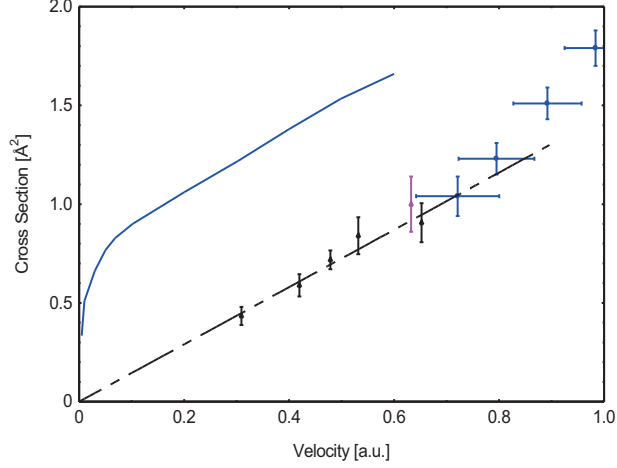$$\sigma^+ = \pi r_{eff}^2 P_{release} \tag{7}$$

**Figure 23:** *The solid curve shows a typical theoretical cross section for single ionization of atomic hydrogen for antiproton impact as a function of the projectile velocity in atomic units. The experimental data are from ref. [20] and show the cross section for creation of $H_2^+$ in collisions of antiprotons with molecular hydrogen. The dashed line is a linear fit to those data.*

This gives the solid curve in figure 23, which agrees well with a multitude of much more refined theoretical calculations [20]. A behaviour much like that for atomic hydrogen was also found for the helium target [21, 22].

If we compare with the data for the molecule, we observe two things: The molecular cross section is proportional to the projectile velocity, a behaviour which is quite unlike the almost flat cross section for the atom, and the molecular cross section is unexpectedly small. This last point can be seen if we regard the cross section at, for example, a velocity of 0.3 a.u. where the molecular cross section is less than half of the atomic one. This should be seen in connection with the fact that the molecule has two ionisable electrons, and that these each are bound with more or less the same energy as the single electron in the atom.

We suggest that the reason for the smallness of the cross section and for the projectile velocity dependence is to be found in the fact that during the collision, when the projectile approaches one of the protons of the hydrogen molecule, there is always another proton which can act as a temporary binding centre for the active electron. Temporarily, therefore, we can have the formation of a $H^-$ - like system, and this hinders ionization. This suppression mechanism has not been seen before. The suppression can be accounted for via the factor $P_{\text{release}}(<< 0.5)$ in equation (1): The more time the active electron has to adjust to the closeness of the projectile, the less likely is ionization, so that

$$P_{\text{release}} \sim \delta(t)^{-1} \sim V_{\text{proj}} \tag{8}$$

Since temporary formation of $H^-$ is part of the suggested model for the suppression of the formation of $H_2^+$, it might be expected that we would observe more fragments, like $H^+$:

$$
\begin{aligned}
H_2 \quad &\rightarrow \quad H_2^+ \\
& \quad\;\; H^+ + H \\
& \quad\;\; H^+ + H^+ \\
& \quad\;\; H^- + H^+
\end{aligned}
$$
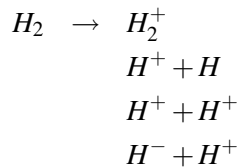
Here, all other channels, except for the first, results in the creation of $H^+$. We show in figure 24 that such
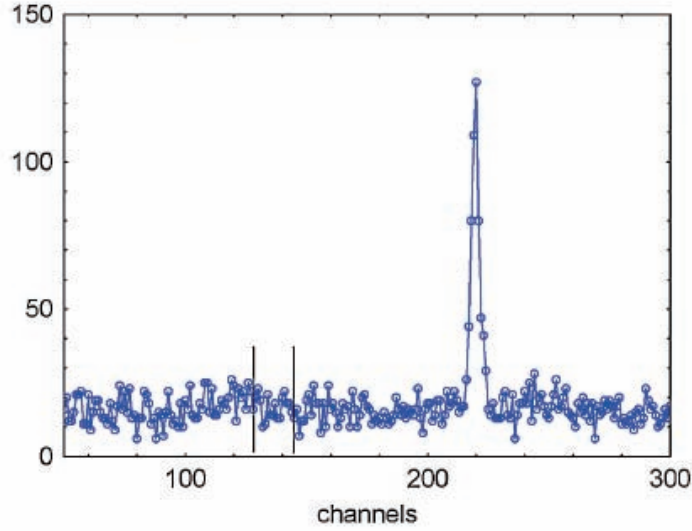
20

**Figure 24:** *An example of a TOF spectrum of the ions created. It was obtained for an impact energy of 10.6 keV. The peak is $H_2^+$ ions. The two vertical lines indicate the TOF interval where $H^+$ ions are expected. One channel is 2.44 nsec. Zero TOF is in channel -70.*

a compensation for the lack of the creation of $H_2^+$ is not found. We therefore observe a real suppression of ionization.

The mechanism proposed here is, we believe, fundamentally the same as the mechanisms which make the stopping power of slow antiprotons proportional to the projectile velocity. For very slow antiprotons we may assume that almost all excitation and ionization events result in energy transfers T around the value of the ionization threshold *I*. We may therefore write:

$$\frac{dE}{Ndx} = \int T d\sigma_T = I\left[\int d\sigma_T^{\text{ion}} + \int d\sigma_T^{\text{exc}}\right] \tag{9}$$

which suggests that $dE/dx$ is proportional to the ionization (excitation) cross section. The only prerequisite needed for having a velocity proportional stopping power for slow antiprotons is, quite possibly, the presence of other atoms nearby. This may explain why all solids investigated yet (having quite different electron structures such as aluminium and lithium flouride) show velocity proportionality [23, 24].

## 5.2 Plans for 2011 and beyond

Since 1986, where the first measurements of ionization cross sections for antiproton impact were performed, we have moved gradually from projectile energies of several MeV to the present few keV, covering collisions where the projectile acted as a small perturbation, over strongly interacting systems to the present quasi-adiabatic collisions. We believe that it will take a quite different experimental approach to investigate collisions at even lower impact energies, and tests have been performed by the ASACUSA collaboration. However, we realise that in the future we need to measure differential cross sections. The reason for this is illustrated in figure 25, which shows calculations by McGovern et al. [25] of the triple differential cross section for single ionization of helium by 3 keV antiproton impact, using the first Born approximation (grid) and a coupled pseudostate model (solid surface). It should be noted that the two theoretical cross sections, integrated over the emission angle are almost identical, whereas the differential cross sections are certainly
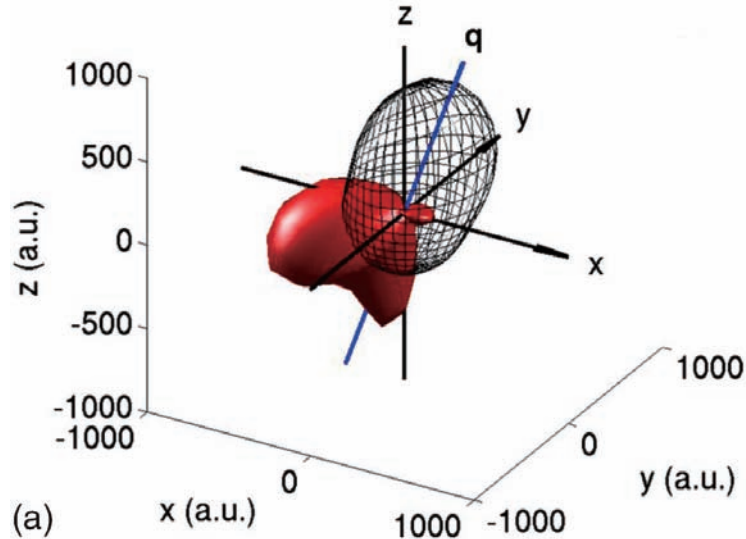
**Figure 25:** *Triple differential cross section for single ionization of helium by 3 keV antiproton impact, using the first Born approximation (grid) and a coupled pseudostate model (solid surface) by McGovern et al. [25].*

not. We shall therefore be in a position to supply the theorists with much more "demanding" experimental data to compare with future theoretical calculations, when such differential cross sections are measured.

For this purpose, the ASACUSA collaboration is considering two experimental approaches: The first consists of the development of a storage device, which will let us "reuse" the antiprotons that pass through our target gas without creating ionization. It will consist of a pulsed acceleration section, which connects the MUSASHI Penning trap to a small electrostatic storage ring. Here, the antiprotons coast around some $10^4 - 10^6$ times, effectively supplying the in-built reaction microscope with a similar factor more antiprotons than is presently available. The other approach is to install a reaction microscope in the planned ELENA storage ring.

# 6   Antiproton-nuclei cross sections experiment at 100 keV

## 6.1   Experiment in 2010.

The main goal of the experiment is the measurement of the annihilation cross sections of antiprotons on nuclei at around 100 keV. In this energy region no data exist while the existing data at 0.5-1 MeV show an unexpected behavior in respect to the dependence on the mass number of the target.

The deceleration of the 5.3 MeV antiproton beam from AD down to 100 keV is performed by the ASACUSA RFQD which is followed by the so-called "dog-leg" momentum selector.

As confirmed by the 2009 experiment, the feasibility of the measurement depends strongly on the possibility to get a reliable beam with a spot having a diameter of few centimeters and no halo in order to avoid annihilations on the ring of the targets.

Multi-particle tracking simulations which accounts non-linear effects such as chromatic aberration have been done by the A.Lombardi's team from BE/ABP and the results were used as starting parameters to tune the beam.

In 2010 the experiment has had 2 different phases.

In the first phase the apparatus is similar to the one used in 2009 with a particular care for the screening from the products of the antiproton annihilations along the beam before the target. A sketch of the exper-

imental set-up is depicted in Fig.26. After the dog-leg and following the antiproton beam path, a concrete wall is placed around the beam line for background suppression followed by a vacuum pump system and then by the cylindrical vertex detector already used for the 5 MeV measurement. The target is at the end of the detector where the target vessel is enlarged in order to move away the annihilations on the lateral wall. The targets can be easily changed by means of a rotary linear multi-motion system. A new beam profile monitor with a grid of electrode pads fabricated on a normal glass-epoxy circuit-board can be placed at the target position for the beam tuning.
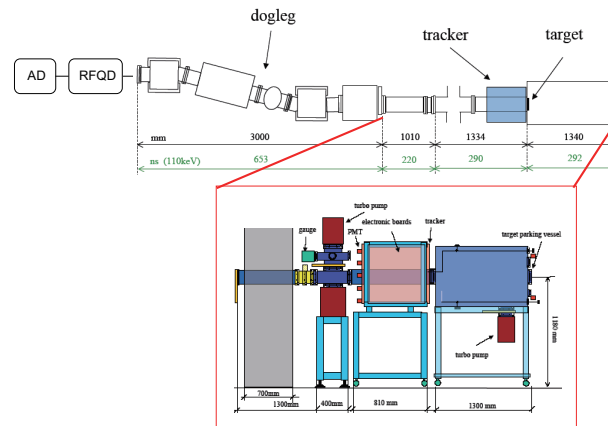


**Figure 26:** *Sketch of the ASACUSA apparatus for σₐₙₙ measurement of p̄ at 110 keV used in the first phase in 2010.*

Many efforts have been devoted for tuning the beam at the best. In Fig.27 the reconstructed vertices of the annihilations on a disk made by 135 nm of formvar on a support ring of 11 cm in diameters are plotted for 110 keV antiprotons. The radial positions indicate that a considerable amount of annihilations are on the thick frame of the target due to the stopped antiprotons of the beam halo. This large spread of the antiproton beam makes the measurement problematic in consideration of the limited statistics achievable.
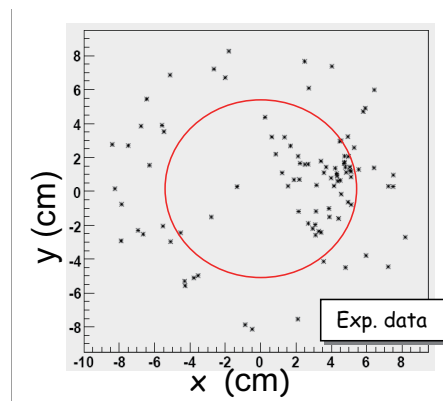


**Figure 27:** *Y- versus x-coordinate of the reconstructed vertices. The red circle represents the inner part of the ring supporting the target.*

However the reduction of the halo is possible by reducing the distance between the target and the end of the dog-leg as confirmed by the experience gained from the antiprotonic helium spectroscopy experiment. The modified apparatus is depicted in Fig.28, where the target has been placed closer to the dog-leg by removing the cylindrical detector and the pump system.

In this second phase of the experiment the strategy of the measurement has been largely changed. The
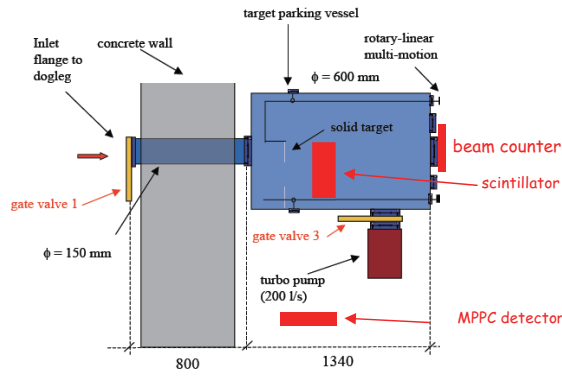
**Figure 28:** *Sketch of the ASACUSA apparatus for $\sigma_{ann}$ measurement of $\bar{p}$ at 110 keV used in the second phase in 2010.*

vertex detector has been abandoned and the detection of the annihilations on the targets comes only from the temporal information recorded by some scintillators devices placed close to the target.

An experimental study of the beam features has been performed in order to verify the actual feasibility of the measurement with the new configuration. The core of the 110 keV antiproton beam measured by the new beam monitor placed at the target position has a spot of 2 cm in diameter. The proximity of the target to the end of the dogleg has permitted a strong reduction of the antiproton beam halo, as shown in Fig.29. The signal colored in red has been recorded by a scintillator close to the target region when the thick ring
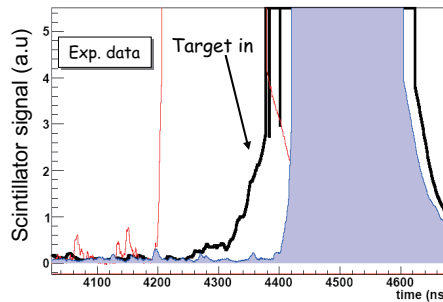


**Figure 29:** *Scintillator signals for different conditions: thick material across the beam (red); only the ring with no target (blue); 135 nm formvar target (black)*

of the target frame has been intentionally rotated across the beam in order to identify the time range where the signals from the target are expected. The signal colored in blue is obtained for the so-called "empty target", that is when the ring with no target has been correctly positioned with its axis coincident with the beam axis. The Fig.29 clearly indicates that beam halo is well confined in a radial region smaller than the dimensions of the target ring, as requested. The black line in Fig.29 is the signal when the formvar target is positioned across the beam. The effect of the presence of the target is evident. But, as confirmed by Monte Carlo simulations (by means of the Geant3 package opportunely modified for the low energy processes) of the beam transport in our apparatus, only a small fraction of the signal in the fiducial time interval is due to antiproton annihilations in the target. Annihilations on the lateral wall of the target vessel coming from the antiprotons scattered from the target are superposed in time to the annihilations in the target as a consequence of the spread in time of the antiproton beam. Even if the reduction of time width of the antiproton beam in AD was possible by operating on the scrapers, the different times of flight along the dog-leg of the different energy components of the beam gives a FWHM of the antiprotons arrival times on the target as large as 110 ns, see Fig.30.

A further reduction of the beam time width can be achieved by putting an iris inside the dogleg which
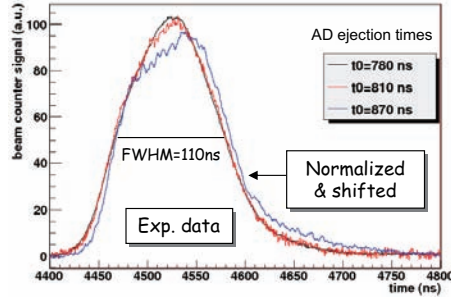
24

**Figure 30:** *Beam counter signals for different ejections times in AD selected by the scrapers. The signals have been normalized and shifted of the nominal delay of the different ejection times.*

increases the monochromaticy of the beam.

In conclusion the new set-up has permitted to avoid the pernicious halo of the beam but, in order to identify in a clear way the annihilations in the target, a larger separation in time from the annihilations on the lateral wall is needed and this can be achieved by increasing the monochromaticy of the beam and/or by increasing the dimensions of the target vessel.

## 6.2 Plans for 2011

The foreseen experimental set-up for 2011 is sketched in Fig. 31. The target vessel has larger dimensions than in 2010: radius is 60 cm (instead of 30 cm) and the length is 2 m (instead of 1.3 m).
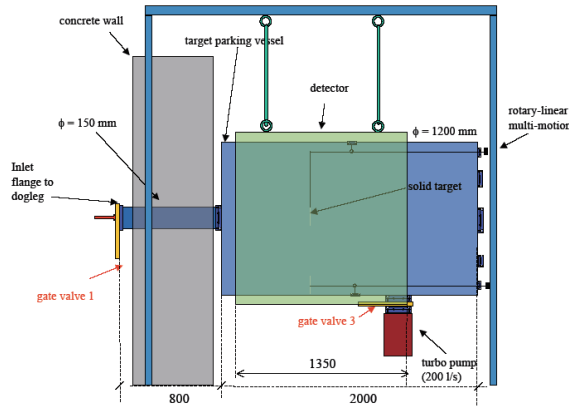


**Figure 31:** *ASACUSA experimental set-up for $\sigma_{ann}$ measurement of $\bar{p}$ at 100 keV for 2011.*

This allows the antiproton annihilations on the target vessel to be separated in time from the annihilations on the target (see Fig. 32) as confirmed by Monte Carlo simulations with Geant3 assuming the 2010 experimental time distribution for the antiproton beam.

The times of the annihilations will be measured by the large modules already used for the antihydrogen experiment with the Cusp trap. In the simple geometrical configuration of Fig. 33, the simulated detection efficiency of the annihilations in the target is around 53% by requiring that at least one charged pion hits one module.

With this configuration the detector can be used also for reconstructing the annihilation vertices with resolution $\sigma_x$=2 cm, $\sigma_y$=8 cm, $\sigma_z$=2 cm but with a reduced efficiency of around 2% due to the stronger request that from each annihilations at least 2 prongs are reconstructed by the detector.
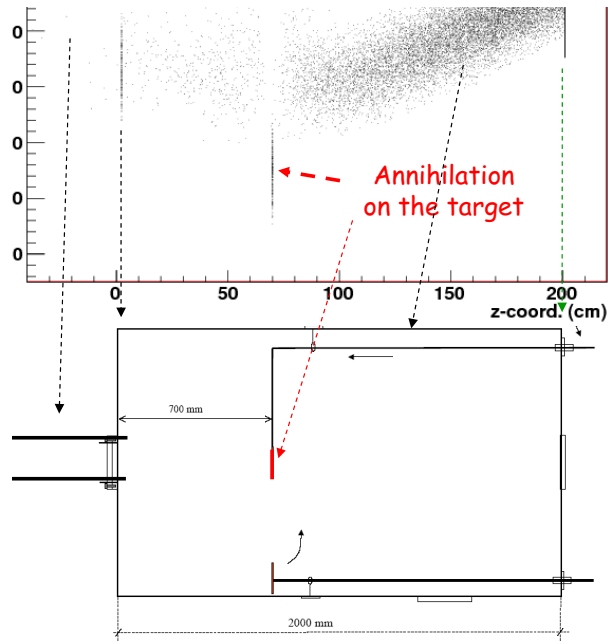
25

**Figure 32:** *Time versus longitudinal coordinate of simulated annihilations in the 2011 set-up for 110 keV antiproton beam on a 70nm thick carbon target.*
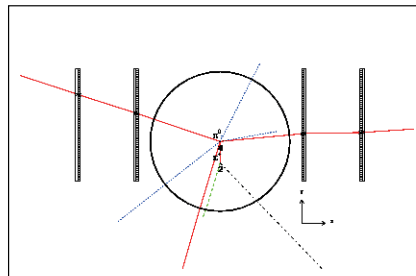


**Figure 33:** *Simulated annihilation event in the target for a possible 2011 geometrical configuration of the detector. The circle represents the target vessel, the thick lines are the 4 modules of the segmented scintillator detector, the red lines are the charged pions inn a typical annihilation event.*

We must point out that the only time information from the modules, with the counting of the beam recorded by a calibrated scintillator at the end of the target vessel, is enough to perform the measurement of the annihilation cross section and that the vertex reconstruction can be performed in parallel without affecting the temporal measurement. The use of the vertex information could give a more stringent check of the disentangle between the antiproton annihilations in the target from the background annihilations outside the target and also useful information on the nuclear and Coulomb scattering.

With the presented configuration the main source of background is due to the annihilations in the target due to antiprotons scattered at about $90^O$ that will go at rest in the target since the 100 keV antiproton range is of the order of microns in solid material. These events cannot be distinguished from the antiprotons annihilations in flight and their contribution must be subtracted by means of reliable evaluations based on the well known Rutherford scattering and stopping power in the considered target. For example in the case

26

of the simulated 70 nm carbon target, their contribution is less that the contribution of the annihilations in flight.

Taking into account the estimated background and with a conservative hypothesis of some $10^5$ of antiprotons per bunch in the single mode extraction of the AD beam, we foresee to acquire some hundreds of in-flight events per day with the only time information.

# References

[1] Y. Enomoto *et al.*, *Phys. Rev. Lett.* **105**, 243401 (2010).

[2] N. Kuroda *et al.*, *Phys. Rev. Lett.* **94**, 023401 (2005).

[3] H. Imao *et al.*, *Journal of Physics: Conference Series* **225**, 012018 (2010).

[4] X.-P. Huang, F. Anderegg, E. M. Hollmann, C. F. Driscoll, T. M. O'Neil, *Phys. Rev. Lett.* **78**, 875 (1997).

[5] H. Saitoh, A. Mohri, Y. Enomoto, Y. Kanai, Y. Yamazaki, *Phys. Rev. A* **77**, 051403 (2008).

[6] M. Amoretti *et al.*, *NATURE* **419**, 456 (2002).

[7] G. Gabrielse *et al.*, *Phys. Rev. Lett.* **89**, 213401 (2002).

[8] G. Gabrielse, S. L. Rolston, L. Haarsma, W. Kells, *Physics Letters A* **129**, 38 (1988).

[9] M. C. Fujiwara *et al.*, *Phys. Rev. Lett.* **101**, 053401 (2008).

[10] T. Gallagher, *Rydberg Atoms* (Cambridge University Press,, 1994).

[11] B. R. Beck, J. Fajans, J. H. Malmberg, *Phys. Rev. Lett.* **68**, 317 (1992).

[12] ASACUSA collaboation, SPSC-P-307 Add. 1, CERN-SPSC2005-002 (2005).

[13] A. Mohri and Y. Yamazaki, *Europhys. Lett.* **63**, 207 (2003).

[14] H. Imao, private communication.

[15] B. Juhász and E. Widmann, *Hyperfine Interactions* **193**, 305 (2009), 10.1007/s10751-009-0016-7.

[16] M. Hori *et al.*, *Phys. Rev. Lett.* **96**, 243401 (2006).

[17] V. I. Korobov, *Phys. Rev. A* **77**, 042506 (2008).

[18] M. Hori and A. Dax, *Opt. Lett.* **34**(8), 1273 (2009).

[19] M. Hori and V. Korobov, *Phys. Rev. A* **81**, 062508 (2010).

[20] H. Knudsen *et al.*, *Phys. Rev. Lett.* **105**, 213201 (2010).

[21] H. Knudsen *et al.*, *Phys. Rev. Lett.* **101**, 043201 (2008).

[22] H. Knudsen *et al.*, *NIMB* **267**, 244 (2009).

[23] S. P. Møller *et al.*, *Phys. Rev. Lett.* **88**, 193201 (2002).

[24] S. P. Møller *et al.*, *Phys. Rev. Lett.* **93**, 042502 (2004).

[25] M. McGovern, D. Assafrão, J. R. Mohallem, C. T. Whelan, H. R. J. Walters, *Phys. Rev. A* **79**, 042707 (2009).

[26] M. Iwasaki et al., *Phys. Rev. Lett.* **67**, 1246 (1991).

[27] T. Yamazaki et al., *Nature* **361**, 238 (1993).

[28] T. Yamazaki et al., *Phys. Rep.* **366**, 183 (2002).

[29] R.S. Hayano et al., *Reports on Progress in Physics* **70**, 1995 (2007).

[30] D. Bakalov and V. Korobov, *Phys. Rev. A* **57**, 1662 (1998).

[31] V. Korobov and D. Bakalov, *J. Phys. B* **34**, 519 (2001).

[32] E. Widmann et al., *Phys. Rev. Lett.* **89**, 243402 (2002).

[33] T. Pask *et al.*, *J. Phys. B: At. Mol. Opt. Phys* **41**, 081008 (2008).

[34] M. Hori et al., *Phys. Rev. Lett.* **96**, 243401 (2006).

[35] V. Korobov and Z.-X. Zhong, *Phys. Rev. A* **80**, 042506 (2009).

[36] V. Korobov, *Phys. Rev. A* **73**, 022509 (2006).

[37] J. Sakaguchi et al., *NIM A* **533**, 598 (2004).

[38] T. Pask et al., *Phys. Lett. B* **678**, 55 (2009).

[39] V. Korobov, unpublished (2010).

[40] G. Korenman, private communication (2010).